

Review

# In Situ X-ray Diffraction as a Basic Tool to Study Oxide and Metal Oxide Catalysts

Olga A. Bulavchenko <sup>1,2,\*</sup>  and Zakhar S. Vinokurov <sup>1,3</sup> 

<sup>1</sup> Boreskov Institute of Catalysis SB RAS, Lavrentiev Ave. 5, 630090 Novosibirsk, Russia; z.s.vinokurov@srf-skif.ru

<sup>2</sup> Department of Physics, Novosibirsk State University, Pirogova, 2, 630090 Novosibirsk, Russia

<sup>3</sup> Synchrotron Radiation Facility SKIF, Boreskov Institute of Catalysis SB RAS, Morskoy 2, 630090 Novosibirsk, Russia

\* Correspondence: obulavchenko@catalysis.ru

**Abstract:** X-ray diffraction (XRD) is a standard technique that is widely applied in heterogeneous catalysis to determine phase composition, atomic structure, and size of crystallites. This review is focused on the application of in situ XRD for studying the catalysts during their “lifetime” (under synthesis, activation, operation, and deactivation conditions), limiting the objects of research to oxide and metal oxide catalysts. Also included is a brief overview of modern techniques and instruments and the latest works illustrating different aspects of this technique in catalyst research. The main conclusion is that the field of heterogeneous catalysis research would benefit substantially from the application of in situ XRD for the structural, phase, and morphological characterization of solid catalysts. Even more useful information can be obtained if XRD is combined with other techniques that are more sensitive at length scales different from that of XRD.

**Keywords:** in situ XRD; operando XRD; catalyst; oxide; metal



**Citation:** Bulavchenko, O.A.; Vinokurov, Z.S. In Situ X-ray Diffraction as a Basic Tool to Study Oxide and Metal Oxide Catalysts. *Catalysts* **2023**, *13*, 1421. <https://doi.org/10.3390/catal13111421>

Academic Editor: Leonarda Liotta

Received: 26 September 2023

Revised: 31 October 2023

Accepted: 1 November 2023

Published: 7 November 2023



**Copyright:** © 2023 by the authors. Licensee MDPI, Basel, Switzerland. This article is an open access article distributed under the terms and conditions of the Creative Commons Attribution (CC BY) license (<https://creativecommons.org/licenses/by/4.0/>).

## 1. Introduction

The development of the modern chemical industry is largely determined by the design of active, stable, and mechanically strong catalysts. A necessary condition for the development of new catalysts is a detailed understanding of the structure of the material and the processes occurring on the surface of catalysts at the atomic and molecular levels.

In order to study the structure of a catalyst in detail, a wide range of methods is commonly used, including X-ray and neutron diffraction, spectroscopy techniques, thermal analysis, adsorption techniques, transmission, and scanning electron microscopy. Heterogeneous catalysis is a surface phenomenon, so the main interest of the researcher is the state of the surface. The catalyst can be in the form of massive solids, but in most cases, nanoparticles of the catalytically active phase are located on the surface of a support. X-ray diffraction (XRD) is best known for its ability to define a bulk structure of crystalline materials. Therefore, the question may arise as to how the results obtained using XRD can shed light on the surface-related catalysis phenomenon. Indeed, XRD struggles with cases when a number of bulk atoms are comparable with ones of the surface (typically for highly dispersed systems, with dimensions < 1 nm), but it still can provide useful information about the support. In many cases, XRD truly shines because the knowledge of the structure of the active phase—composition, lattice constants, strain state, atomic arrangement, and defect structure—can be invaluable for any reasoning about the active state of the catalyst. Moreover, the changes in the bulk nanostructure will affect the surface structure through the gradient of bulk lattice energy to the surface free energy. The specific changes in the defect structure also may affect the surface reordering. That is, before studying the state of the surface, it is necessary to know the structure of the foundation on which the catalysis phenomenon occurs.

The traditional approach to studying the catalysts involves catalytic tests and ex situ characterization of the catalyst before and after the reaction by various methods. The obvious disadvantage of this approach is that ex situ studies are performed under conditions far from the working conditions of the catalytic process, which usually proceeds at relatively high temperatures and pressures in the presence of gas/liquid reagents and products of the catalytic reaction. For ex situ characterization, it is impossible to study the active state of the catalyst and reaction intermediates. It is worth emphasizing that the state of the catalyst can be changed significantly under the reaction conditions due to the interaction with reagents and the effect of high temperature and pressure. The catalyst may undergo transformations that drastically modify its composition, morphology, and crystal structure. For example, during the extraction of the catalyst from the reactor after the catalytic process, the interaction with atmosphere oxygen could cause reoxidation and, as a result, make the determination of the active state of the catalyst impossible. Therefore, it is necessary to study catalysts under conditions as close as possible to the conditions of their activation/deactivation and operation.

In the literature, there are two terms commonly used to denote studies of catalysts performed in non-ambient conditions: *in situ* and *operando*. Currently, the *in situ* term is the most popular and has been actively used since the 1950s. According to the SCOPUS® database, one of the first *in situ* XRD studies of catalysts is the study of iron-containing catalysts for ammonia synthesis, published in 1951 [1]. The term *operando* has been actively spreading in the literature for the last two decades and has a narrower application. In the context of catalysis, it was first mentioned in the study of supported metal oxide catalysts by Raman spectroscopy in 2002 [2] and was used to describe experiments under the conditions of a catalytic reaction. In other words, it means studying the catalytic and structural properties of the catalyst simultaneously. Also, terminology such as high-temperature/pressure, time-resolved, and non-ambient XRD is often used in publications to denote “non-standard” conditions.

This review was performed using the SCOPUS® search engine. Preliminary search for diffraction studies of catalysts (TITLE-ABS-KEY ((“X-ray diffraction” OR “XRD”) AND (“catalytic” OR “catalysis” OR “catalyst”))) by title, abstract, and keywords returned 141,440 documents as of August 2023, with about 1% of publications being older than 1988. Subsequent limiting by non-ambient XRD (TITLE-ABS-KEY ((“X-ray diffraction” OR “XRD”) AND (“catalytic” OR “catalysis” OR “catalyst”)) AND (“*in situ* XRD” OR “*in situ* X-ray diffraction” OR “non ambient XRD” OR “non ambient X-ray diffraction” OR “high temperature XRD” OR “high temperature X-ray diffraction” OR “*operando* XRD” OR “*operando* X-ray diffraction”)) AND PUBYEAR > 1987) produces 1099 articles, with only 53 that are referred to “*operando*”. To compare and demonstrate trends, these data are presented together with publications that are not limited to the field of catalysis (Figure 1). Obviously, only about 10% of publications about catalysts (141 k vs. 1.3 M) having XRD data is not relevant because X-ray diffraction is a standard characterization technique for materials science, together with BET surface analysis and electron microscopy. However, the search is limited by only an abstract, title, and keywords, and standard techniques are often not mentioned by the authors in these fields. Still, the search for non-ambient techniques should provide more relevant results (terms should be present in the search fields) because, typically, the article is based on the data obtained by *in situ* or *operando* XRD if applied. The “*in situ* XRD<sub>cat</sub>” and “*in situ* XRD” show similar trends and slightly slower growth compared to the “XRD<sub>cat</sub>”. The growth that “*operando* XRD” and “*operando* XRD<sub>cat</sub>” have shown in recent years is most likely due to the growing popularity of the term.

*In situ* XRD is a useful analytical tool in solid-state chemistry and physics and allows one to analyze phase transformations, solid–solid, solid–gas, and solid–liquid reactions, formation of intermediates, and study the kinetics of processes. It is worth noting that about 10% of publications containing “*in situ* XRD” are related to the study of catalysts. These works cover different aspects of the catalyst life: synthesis and activation—phase

transformations during oxidation/reduction; study of the active component of the catalyst under reaction conditions; and study of deactivation processes. Studies on catalyst supports and their interactions with the catalysts can be singled out in a separate area of research. Studies are divided into cases where only the use of the in situ XRD method provides the main scientific result and others when in situ XRD is used to complement other methods.

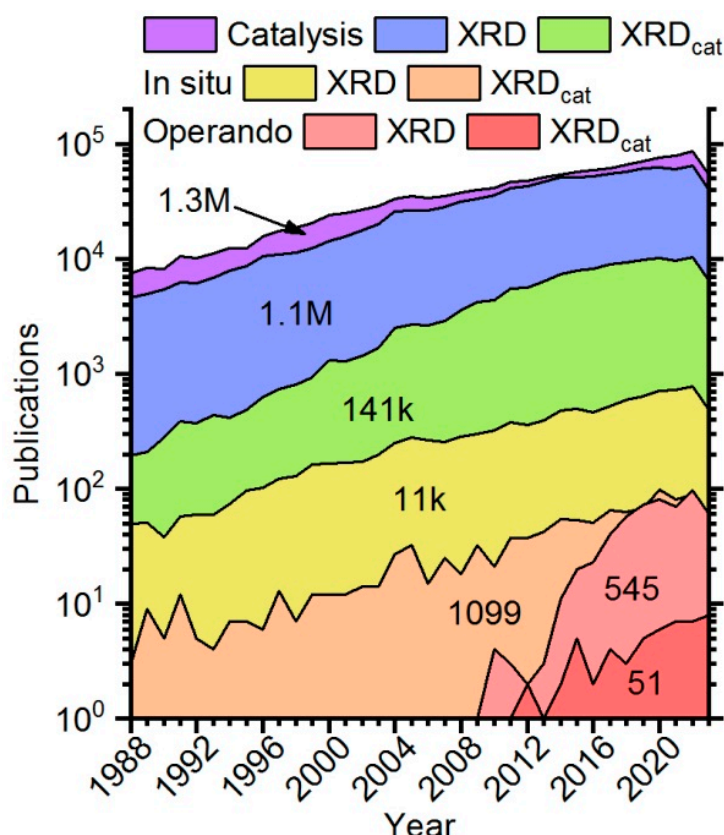


**Figure 1.** Annual publication activity for all catalytic studies (violet), catalytic studies performed using XRD (green), in situ XRD (orange), and operando XRD (red). For comparison, all XRD studies (blue), in situ XRD (yellow), and operando XRD (pink) are presented. Numbers indicate publications of a certain topic in total.

Of course, there are various processes that can change the catalysts' structures and, therefore, require applications of in situ approaches to study. This review is focused on the processes of loss and uptake of oxygen, limiting the objects of research to oxide and metal oxide catalysts. Here, we will provide a brief overview of the latest works illustrating different aspects of the application of in situ XRD for studying mentioned catalytic systems. This review is divided into two sections: (1) techniques and instruments applied for in situ XRD and (2) application of in situ XRD to characterize various catalysts and model systems at different stages of their “lifetime”.

## 2. Techniques and Instruments

One of the first non-ambient or in situ diffraction experiments was the study of “silicon steel” (iron containing 3.5% silicon) at temperatures from 77 to 1273 K conducted by Albert W. Hull in 1917 (General Electric Research Laboratory, USA) [3]. In his work, he also stated the very basic principles of the powder diffraction technique that are still relevant today; for example, “Disorder, as regards orientation of the small crystals, is essential. It is attained by reducing the substance to as finely divided form as practicable, placing it in a thin-walled tube of glass or other amorphous material, and keeping it in continuous rotation during the exposure”. Over the past 100 years, diffraction methods and instruments have been actively developed

and have become widely used in the fields of materials science. Here, we present a brief introduction to the basic instruments of the researcher: X-ray diffraction techniques, X-ray sources, X-ray detectors, reaction chambers/cells, reaction products analysis, and X-ray data analysis techniques.

### 2.1. Diffraction Techniques

X-ray diffraction is a powerful tool for structure characterization, but it needs to be carefully applied in the field of heterogeneous catalysis because catalytic reactions occur at the surface of a catalyst, and XRD is usually applied as a bulk-sensitive method. However, in most cases, the volume structure correlates with the morphology and surface properties of the catalyst, and changes in the bulk structure may shed light on the surface properties. Therefore, the XRD research in the field of catalysis can be divided into two basic groups:

- The bulk structural research—This is quite useful for getting general information on the bulk catalyst/support (phase, structure, and crystallinity), including the changes caused by the sample environment (reaction, temperature, etc.) during synthesis, activation, or reaction studies;
- More sophisticated approaches include when the information on the surface structure/composition is either obtained indirectly by combining the XRD data with the data obtained via different surface- or element-sensitive techniques (XPS [4], XAS [5], IR-/UV spectroscopy [6,7], STEM-EDX [8], SOR [9] etc.) or directly using grazing incidence diffraction optionally with microfocused beams (generally requires a synchrotron and mostly limited by a model atomically flat systems) [10,11].

In a significant number of cases, the catalysts exhibit weak or no diffraction patterns due to a nanocrystalline nature; usually, a few unit cells or about 1 nm is a critical dimension. Even though they are not detectable by a standard XRD experiment, still information about short-range ordering could be obtained by the pair distribution function technique (PDF) [12]. In addition, the small/ultra-small angle X-ray scattering technique (SAXS/USAXS, including anomalous ones) can be utilized for studying larger scales like size and shape distributions of particles [13,14]. The high sensitivity of the bulk XRD to the deviations from the perfect order (defects) is also useful in the field of catalysis research because ordering/clustering of these defects can drive structural transformations, which is a common case for *in situ*/operando studies [15–17].

There are features of *in situ*/operando studies that are important both for the experiment itself and for data handling. The catalysts are the dynamic systems that are sensitive to the reaction environment, temperature, and pressure, and obviously to how fast the latter is changing. Researchers, when handling data on changes in lattice parameters, need to consider not only TECs but also the chemical expansion that can be caused by thermodynamic factors, oxidation/reduction of the sample, and defect ordering [18,19]. Even in the case of a quasistatic reaction, there could be a local overheating that affects the obtained results. To exclude the possible errors, careful heat calculations, the dilution of catalyst/reaction mixture, or effective heat transfer supports/gas carriers are required [20,21]. The temperature and reaction product measurements are strongly dependent on “where? how? and how fast?” they are measured, especially when fast kinetic processes are involved [22–24]. Speed and completeness (diffraction angles) of the diffraction data collection also need to be carefully considered for *in situ*/operando studies because the state of the sample may change during one diffraction pattern measurement (extremely important when scanning with a detector). The changes in the volume of the sample caused by thermal or reaction factors may add some complexity to the data processing, for example, changing the scattering plane position in Bragg–Brentano geometry (requires using the parallel-beam geometry or internal standard [25,26]). Scattering of the X-rays on the environment or chamber/cell parts is another effect contributing to the diffraction pattern. Typically, this is solved by performing a “blank” experiment, but it needs to be considered when, for example, the sample environment (in terms of scattering, denser gas/liquid) changes during the experiment [27]. Switching between different carrier gases, for example, from lighter helium

to heavier argon, during an experiment can affect the quality of data. Fluorescence from the sample/chamber could be another reason for the low signal-to-noise ratio and high background (common case for a characteristic X-ray scattering setups); usually, the problem is solved by changing the X-ray source energy and using energy dispersive detectors or fluorescence filters [28].

## 2.2. X-ray Photon Sources

Typically, the X-ray photon sources are divided into two groups:

- Large-scale facilities based on either the linear accelerators—free electron laser facilities such as XFEL (<https://www.xfel.eu/> (accessed on 2 November 2023)), SLAC (<https://lcls.slac.stanford.edu/> (accessed on 2 November 2023)), etc.—or circular particle accelerators, i.e., synchrotron facilities such as MAX VI (<https://www.maxiv.lu.se/> (accessed on 2 November 2023)), ESRF (<https://www.esrf.fr/> (accessed on 2 November 2023)), Diamond (<https://www.diamond.ac.uk/> (accessed on 2 November 2023)), etc., where the radiation is emitted by accelerating particles (usually electrons);
- Tabletop X-ray sources mainly use the method to generate X-rays by the interaction between accelerated electrons and matter.

The advantages of the large-scale facilities are the unique properties of the obtained photons. The time structure of the X-ray pulses of FELs (femtosecond X-ray experiments, FXE) allows for the study of the elemental steps of chemical reactions in timescales of chemical bond breaking and formation, but still, in the majority of these experiments, spectral approaches are used. The operando powder diffraction applications are limited by the liquid phase catalytic experiments due to the high radiation/thermal damage, and the gas phase catalysis is practically impossible [29,30]. FELs are mainly used for serial femtosecond crystallography (SFX) experiments, where the diffraction of individual crystals is collected before the crystal is damaged [31]. In the case of synchrotron facilities, the insertion devices (wiggler, undulators, etc.) generate a wide energy spectrum (from tens to thousands of eV) of high brilliance (up to  $10^{22}$  ph/s/0.1 b.w./mm<sup>2</sup>/mrad<sup>2</sup>) [32]. This is beneficial for catalytic experiments due to the higher penetration depth (high-intensity hard X-rays), allowing operando studies in reactors close to industrial ones [33], and for the use of modern hybrid photon counting (HPC) area detectors with much faster data acquisition times (up to 24 kHz for Spectrum LAMBDA detectors (<https://x-spectrum.de/> (accessed on 2 November 2023))), allowing the time-resolved operando experiments [34].

The drawbacks are obvious: the cost of such a facility, experimental time limits, and the localization. To perform an experiment, the researcher needs to submit the proposal and compete with other scientists for the time to conduct experiments. If successful, the researcher needs to carefully plan travel to the installation location and the experiment to obtain the most benefit from the limited experimental time.

The tabletop sources are more common, compact, and cheaper. The most widespread are the solid anode X-ray tubes working either with characteristic photons or with bremsstrahlung spectra (typically for microfocus radiography or medical applications). The very principle of X-ray generation limits its flux with the amount of heat generated when the electrons strike the anode. Several technological steps have been taken to overcome these limitations [35] of X-ray tube manufacturing over the decades since their first use by Roentgen in 1895: thermo-ionic filament (Coolidge, 1913); line focus (Goetze, 1919); rotating anode (Bowers, 1929); heat- and shock-resistant metal-ceramics (1980); liquid vacuum bearings (Philips, 1989); anode-grounded tubes (Varian, 1998); rotating frame tubes (Siemens, 2003). Some interesting results were achieved by Excillium (founded in 2008) with a metal-jet technology where the liquid–metal anode is used (either gallium or indium alloys). By excluding the classical power limit of X-ray tubes, they were able to significantly outperform conventional solid anode sources at micron spot sizes (5–40  $\mu$ m source diameter) (<https://www.excillium.com/> (accessed on 2 November 2023)).

Some attempts were made to fill the gap between the tabletop sources and large-scale facilities. The Mirrorcle prototype was reported by Yamada in 1998 [36], combining the

X-ray tube and synchrotron source principles—a small target is placed in the compact electron storage ring, and the bremsstrahlung emission is defined by the energy of the electrons (up to 5 MeV). Still, no commercial success was achieved ([https://www.photon-production.co.jp/en/news\\_index\\_e.htm](https://www.photon-production.co.jp/en/news_index_e.htm) (accessed on 2 November 2023)).

### 2.3. Detectors

The principle of detection of X-ray photons is based on the matter–photon interactions, the most important of which are photoelectric absorption, Compton scattering, and electron–positron pair production [37]. Based on these interactions, the output signal of the detector can be produced by primary ionization, thermal changes, or scintillations. Ionization-based detectors are divided into three groups: the solid state detectors directly converting photons into electric charge (a-Se or a-Si photoconductors, flat panel detectors [38], hybrid photon counting HPC detectors [39]), gas ionization chambers (wire or multi-wire proportional chambers [40]), and imaging plates, where the photon excited states are trapped in the storage phosphor material of the plate and then released by a laser as fluorescent light [41]. The thermal effect of the X-rays absorbed by the high-Z, high-density material could be converted into electrical signals by the Seebeck effect [42]. Scintillator-based X-ray detectors sequentially convert photons into visible light and then into electrical signals using photodetectors (charge-coupled device CCD and complementary metal oxide semiconductor CMOS detectors [43]).

Detectors are also classified by coverage into three types: point (0D), linear (1D), and area (2D). Typically, one must obtain every piece of useful information from photons scattered by the sample; this is especially crucial when it is an X-ray exposure-sensitive case (organic crystals, high photon flux). The use of an area detector not only speeds up the experiments and makes available the time-resolved studies but also excludes experimental errors in the orientation and polarization-sensitive studies (typical for common Bragg–Brentano geometry and position-sensitive linear PSD or point detectors). That is why area detectors are almost always preferable despite the high cost. Some exceptions are the cases when one requires the higher resolution at the expense of experiment time (analyzer crystals [44,45]) or energy-dispersive X-ray diffraction studies (silicon or germanium solid state detectors [46]); both greatly benefit from using the synchrotron source. Currently, the dominant type of detectors for small-angle scattering, surface, and powder X-ray diffraction are the hybrid photon counting (HPC) ones, especially for the synchrotron applications (most common are based on the CERN Medipix and Timepix technology [39], including Dectris (<https://www.dectris.com/> (accessed on 2 November 2023)), X-spectrum (<https://www.pitec.co/> (accessed on 2 November 2023)), PiTec (<https://www.pitec.co/> (accessed on 2 November 2023))). In the X-ray energy range from 2 to 100 keV, HPC detectors drastically outperform CCD detectors in terms of their low readout noise (down to one photon), large dynamic range (virtually infinite within the maximum frame rate, up to  $10^{11}$  for the common setups), and image plates by orders of magnitude and lower readout times (up to  $10^8$  ph/s/pixel) [47,48].

### 2.4. Cells and Reactors

The cells and reactors for *in situ*/*operando* XRD studies come in a variety of types, depending on the research being conducted. The specific design will depend on the many parameters of the photon source, technique, detector, and process conditions in terms of temperature, pressure, etc. For example, to study the interface between the cathode and the electrolyte of the solid oxide fuel cell by anomalous XRD technique [49], the researcher requires the following: from the source, they need to be able to switch between the energy absorption edges of elements of interest and to have hard enough intense, focused X-rays to reach the buried interface; from the process conditions, they need to be able to precisely control the oxygen pressure, temperature, and voltage of the cell; from the reactor materials, they need to be resistant to the environment conditions and have minimal interference with the incoming and scattered X-rays; and from the detecting system, they need to maximize

the collected data and minimize the background noise including fluorescence. The main difficulties arise when extreme conditions are required: very high (>1300 K) or very low (<4 K) temperature, high pressure (>10 bar), corrosive environment (acidic or alkaline), and a combination of these. For example, the use of diamond anvil cells (DACs are devices that can achieve ~1 GPa pressure and 1300 K temperature in common cases and up to several thousand degrees temperature and up to ~1 TPa pressure when using laser-driven dynamic-compression diamond anvil cells [50]) requires hard and focused X-rays due to the very small experimental volume (down to tens of microns) and requirements to penetrate materials of the cell, as well as limited achievable scattering angles.

The tabletop setups use a variety of stages depending on the diffractometer; typically, every manufacturer either designs its own stages (Bruker AXS, Billerica, MA, USA (<https://www.bruker.com/en/> (accessed on 2 November 2023)), STOE, Darmstadt, Germany, (<https://www.stoe.com/> (accessed on 2 November 2023))) or makes its equipment compatible with the existing specialized suppliers (Rigaku, Tokyo, Japan, (<https://www.rigaku.com/> (accessed on 2 November 2023)); Thermo Fisher Scientific Inc., Waltham, MA, USA, (<https://www.thermofisher.com/> (accessed on 2 November 2023))). Anton Paar GmbH, Tokyo, Japan (<https://www.anton-paar.com/> (accessed on 2 November 2023)), is a well-known leading supplier of non-ambient stages compatible with common diffractometers for XRD and SAXS studies today. Their portfolio includes reactor chamber XRK900 for solid-state and solid-state gas reactions up to 900 °C and 10 bar, low-temperature chamber TTK 600 with an antechamber option that allows safe transfer of air-sensitive samples, and cryo and humidity chamber CHC plus<sup>+</sup> for controlled relative humidity studies from 10 °C to 80 °C. Bruker AXS has some similar positions, including capillary (TC-TRANSMISSION, up to 1000 °C), humidity (TC-HUMIDITY, −5–75 °C, 5–95% RH), low-temperature (MTC-LOWTEMP, down to −180 °C), and high-temperature (MTC-FURNACE, up to 1100 °C in the oxidative atmosphere) stages. The most suitable tool to study catalysts during catalytic reactions or activation/deactivation is the XRK900 chamber due to the chemically resistant ceramic sample holder and ability to work in a flow regime that complements the XRD data with mass spectrometry/gas chromatography of the reaction products [4]. The most challenging thing in the development of the universal catalytic reactor for XRD experiments is the selection of materials that require low X-ray absorption (X-ray windows, usually beryllium or carbon), enough hardness to work at low/high pressure (from vacuum to tens of atmospheres), and that they are chemically (oxidative environment, hot water vapor or corrosive gases) and thermally resistant (up to 1000 °C). That is why, in some cases where the commercial cell materials are catalytically active, research teams make cells of their own design that are more suitable for the process being studied [51].

The most common types of chemical reactors that are used at synchrotron beamlines for powder XRD or SAXS techniques are either flow or closed quartz capillary cells that are heated (or cooled in a cryo stream) by a flow of gas or placed in the heating block. There are some commercial capillary cells, including Linkam HFSX350V-CAP [52] and Anton Paar HTK 1200 N [53], but mostly the experimental setups are made by beamline groups. There is also a tendency to combine several techniques to obtain maximum data from a single experiment, for example, XRD and IR spectroscopy [54] or XRD and XAS [55]. This adds limitations to the design and construction materials of the cell and to the experimental setup as a whole (X-ray source, detector systems). In the practice of operando research, the creation of a universal cell is impractical and sometimes impossible; either the adaptation of existing equipment to the studied process or the development of a specific cell is required. Still, the experimental capabilities of the synchrotron research facilities are quite exceptional and, for example, allow for the study of the components of an internal combustion engine during its operation by XRD and imaging [56] or to measure the temperature and XRD of a catalyst fixed bed with a spatial resolution gas composition [24] (see Figure 2).

## 2.5. Reaction Products Analysis

For any operando diffraction study of catalysts or catalysts precursors, the characterization of reaction products is crucial for a better understanding of the reaction mechanism.

The most common time-of-flight mass spectrometry (TOF MS) is used to perform the chemical composition analysis. The electron ionization of molecules for MS analysis is typically employed, but due to significant fragmentation, it is less applicable in the case of complex organic compounds. To overcome these limitations, various soft ionization techniques have been developed, including chemical ionization [57], field ionization [58], vacuum UV photoionization [59], and laser ablation resonance-enhanced multiphoton ionization [60]. For a high-resolution gas separation, gas chromatography (GS) is used before MS analysis. A major drawback of implementing GS is the larger data acquisition times changing from seconds for MS to tens of minutes for conventional GS. In the last decade, fast gas chromatography has received renewed attention with successful commercialization for LC–MS/GC–MS instrumentation. Several methods have been developed for faster GS separation, mainly narrow bore columns [61], micro-bore columns [62], and vacuum outlet conditions [63]. The fastest GC applications with relatively high practical utility reported lasting between 1 and 3 min [64].

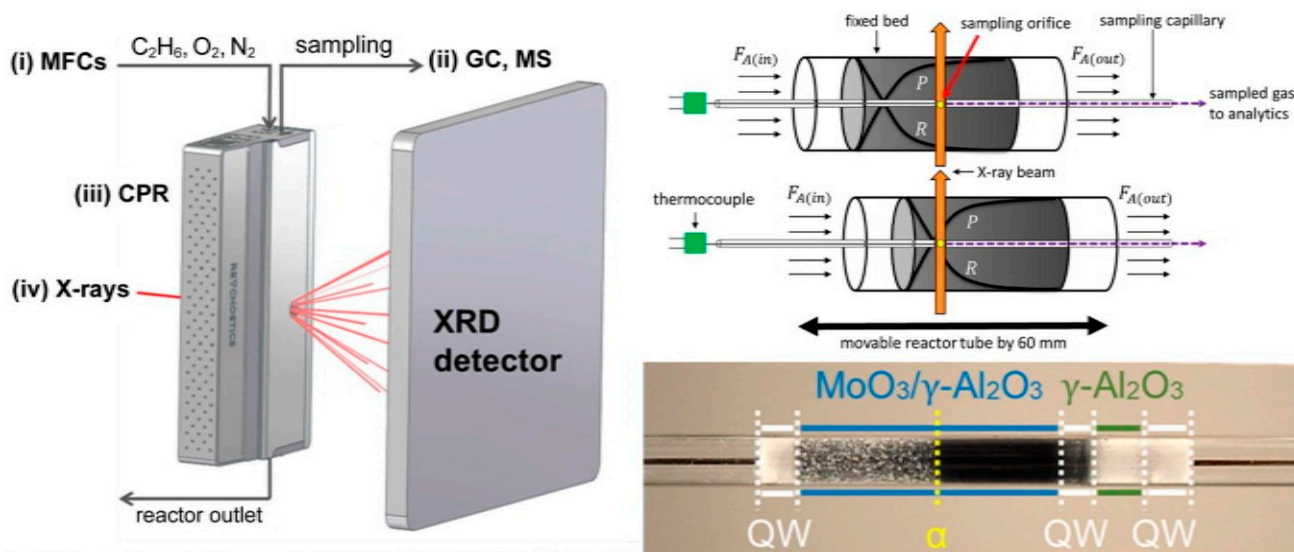


**Figure 2.** Experimental setup for operando XRD spatial profiling (left). Principle of operation and reactor tube loaded with catalyst (right) (QW—quartz wool; yellow line marks the change in the color of catalyst). Reproduced from [24].

## 2.6. X-ray Diffraction Data Analysis

XRD data analysis typically starts with qualitative phase analysis. Phase identification or search–match analysis is based on the “fingerprinting” technique when each unique crystal structure generates a unique diffraction pattern. The usage of powder diffraction databases (the most known ICDD PDF 4+ database contains almost half a million entries [65]) together with dedicated search–match software (an extensive list is provided in reference [66]) allows for relatively fast phase identification, which has been well developed over the past years. Along with the phase analysis, the size of particles is a key characteristic of catalyst [67–69]. The Scherrer equation is commonly used to estimate crystallite size (effective length of diffraction coherence, which is obtained in the direction of the diffraction vector) using the integral breadth of the XRD peak [70]. Large particles may contain several crystallites or domains with different orientations, and it is important to compare crystallite sizes with those obtained with other methods. Since the reflection width is affected by both microstrains and crystallite size, it is important to distinguish between their contributions. In this case, a Williamson–Hall method is often applied to estimate “mean values” of crystallite size and strain [71]. Refinement of structure is a more complex process that is most commonly solved by using a full profile analysis, also known as the Rietveld method [72]. The idea relies on the refining of a set of parameters contributing to the peak’s shape and

position by the least-squares method, matching the modeled and experimental patterns. These parameters include crystal lattice and symmetry, crystal structure, microstructure, background, instrumental factors, and others. Another challenge lies in the amount of data generated during *in situ* experiments, which increases constantly (tens of thousands of diffraction patterns for one synchrotron experiment). That is why batch processing of data in order to decrease its quantity without losing any essential information is crucial. Ideally, the beamline software needs to reduce data (integration over area and time, corrections of the intensities/background), analyze it (batch processing using Rietveld or LeBail, when the set of parameters from the previous calculation is the starting set for the next), and visualize it for the researcher to make decisions of process corrections “on the fly” [73,74]. Ref. [66] covers almost all available software (at the moment) for profile analysis. Usually, *in situ/operando* data do not have enough quality to solve an unknown structure, so the powder indexing technique is out of the scope of this review.

In the last decade, successful attempts were made to develop the algorithms of phase identification and structure refinement using machine and deep learning [75–77]. The advantage of this approach compared to the conventional match algorithms is that the rules are based on the neural network training data. Therefore, an expert could develop the model not only to identify phases but also to predict different parameters that cause deviation from the database, such as lattice parameter discrepancies owing to solid solution. Recent works show that machine- and deep-learning models can be applied to screen novel thin-film materials during early-stage high-throughput material development [77] and for MOF structure identification [76]. One of the features of the neural network approach is the possibility to use large amounts of cheap synthetic data together with small batches of expensive experimental data to achieve accurate phase predictions, as was shown for a Li-La-Zr-O quaternary system [78].

### 3. Application of In Situ XRD for the Characterization of Different Steps of Preparation, Activation, Operation, and Deactivation

In this section, typical *in situ* XRD experiments on catalysts and model systems will be discussed. Works illustrating various aspects of the application of *in situ* X-ray diffraction to study catalysts will be divided into four topics: (1) catalyst synthesis; (2) activation process of catalyst and reduction of model oxides, (3) *operando* research, i.e., under reaction conditions; and (4) deactivation of catalysts.

#### 3.1. Study of the Preparation Procedure

The process of the development of new catalysts with certain properties such as activity, selectivity, and stability typically contains the following cyclic steps: synthesis → catalyst tests → change in synthesis parameters → new synthesis, etc. This evolutionary approach takes a lot of time, resources, and some luck. Characterization of the catalyst at every step and structure–performance modeling (see Figure 3) are highly desirable and provide a lot of information that is useful for planning and optimizing synthesis procedures, thereby saving time and resources. *In situ* studies are optimal in that case because they could provide knowledge about the characteristics of catalysts under non-ambient conditions, covering synthesis, activation, reaction, and stability performance.

Tunable parameters of the catalyst are morphology, phase composition, crystalline and particle sizes, defects, and surface structure. These parameters can be controlled by synthesis conditions—changing initial reagents composition, preparation method, temperature, and pretreatment atmosphere. Usually, the application of *in situ* XRD to the investigation of the synthesis procedure includes the final steps of catalyst preparation covering transformations in solids or the crystallization process. These include, among others, studies of calcination steps, temperature pretreatment of the catalyst precursor in various media (inert gas, reducing environment) [79–84], and hydrothermal treatment [85,86].

In the case of noble metals, the decomposition of precursors in various gaseous media and the changes in phase composition and crystallite size are often studied [79–81].

Baylet et al. [79] investigated the decomposition of palladium oxide supported on  $\gamma\text{-Al}_2\text{O}_3$  at atmospheric pressure under different atmospheres ( $\text{H}_2$ ,  $\text{CH}_4$ , He). In situ XRD showed that the reduction behavior depends on the reducing agent:  $\text{H}_2$  can reduce  $\text{PdO}$  particles at much lower temperatures than methane, while  $\text{PdO}$  decomposition into  $\text{Pd}$  in an inert gas (He) occurs only above 700 °C. In turn, this affects the morphology of both the  $\text{Pd}$  particles and oxide support and, thus, the catalyst performance.

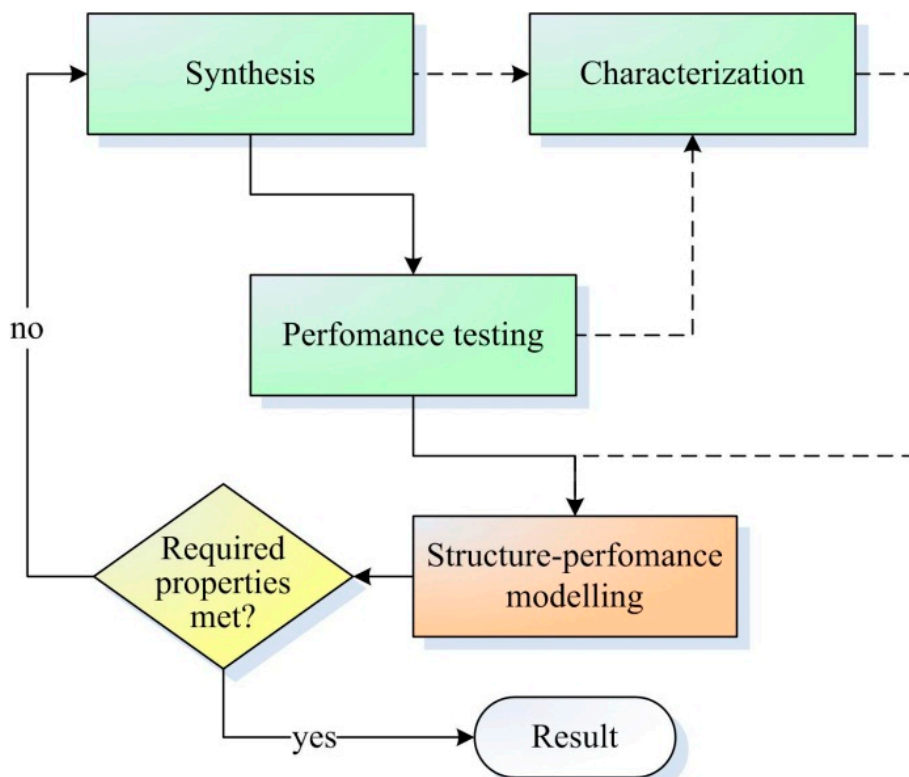


**Figure 3.** Basic workflow diagram of the production of a new catalyst.

Molybdenum-based oxides are promising catalysts for selective oxidation of light alkanes. They have a broad structural variety due to the ability to form shear structures with close composition and incorporate metals from the IV and V groups of the periodic table. The phases formed in such catalysts are determined by the composition and preparation conditions, in particular, by temperature treatment conditions. In situ XRD was applied to study the formation of an active phase in catalysts during thermal treatment in air and in helium for Mo-V-Te-Nb [82,83] oxides. Girgsdies et al. [83] have shown the formation of the crystalline phases M1 (ICSD 55097), M2 (ICSD 55098), tetragonal  $\text{M}_5\text{O}_{14}$  ( $\text{M}=\text{Mo, V, Nb}$ ), and orthorhombic  $\text{MoO}_3$  during thermal treatment of the amorphous precursor. Based on the in situ XRD data, the authors concluded that phases M1,  $\text{M}_5\text{O}_{14}$ , and  $\text{MoO}_3$  are formed competitively, and the final composition of the catalyst is affected by the availability of residual tellurium.

For  $\text{MnO}_x\text{-Al}_2\text{O}_3$  catalysts, in situ XRD was applied to explain a sharp growth of the catalytic activity in oxidation reactions after calcination at 950–1000 °C [87]. The thermal activation effect is quite unusual to observe because, after a high-temperature treatment, the active component becomes dispersed, although it is expected to become sintered [87]. In situ XRD study has shown that at the synthesis temperature, the  $\text{Mn}_{1.5}\text{Al}_{1.5}\text{O}_4$  mixed oxide with the spinel structure is formed. At high temperatures, mixed oxide is a thermodynamically stable compound; upon cooling in air, the oxide decomposes with a release of catalytically active nanoparticles of manganese oxide  $\text{Mn}_3\text{O}_{4+\delta}$  containing weakly bound oxygen [88]. Studies of model  $\text{Mn}_{1.5}\text{Al}_{1.5}\text{O}_4$  oxide revealed that the segregation of the catalyst precursor

is driven by the addition of oxygen and subsequent oxidation of manganese cations [89,90]. Modification of  $\text{MnO}_x\text{-Al}_2\text{O}_3$  catalysts with Ga decreases the catalytic activity. The in situ XRD data indicate that at high temperatures, a solid solution  $(\text{MnGaAl})_3\text{O}_4$  is formed; however, its further segregation upon cooling is hindered. The introduction of gallium stabilizes the structure of the  $(\text{MnGaAl})_3\text{O}_4$  mixed oxide, and the amount of active  $\text{Mn}_3\text{O}_4$  particles and/or weakly bound oxygen produced after decomposition during cooling is much lower, which, in turn, adversely affects the catalytic properties [91].

Another typical study of the catalyst synthesis by means of in situ XRD includes the decomposition of precursor, such as formation of nickel oxide from  $\text{Ni}_3(\text{NO}_3)_2(\text{OH})_4$  [92], copper oxide from copper nitrate [93]; transformation of  $\text{CeCO}_3\text{OH}$  to  $\text{CeO}_2$  [94]; decomposition of Ce and Mn oxalates to mixed Mn-Ce oxides [95]; preparation of  $\text{WO}_x\text{-CeO}_2$  catalysts [96]; formation of Pd-containing zirconia oxide from amorphous precursor [97]; thermolysis of  $[\text{Pt}(\text{NH}_3)_4]\text{CrO}_4$  complex [98], preparation porous mixed-valent manganese oxides by hydrothermal treatment of layered precursor [99], by thermal decomposition of  $\text{KMnO}_4$  [100].

### 3.2. Study of the Process of Activation of Catalysts and Reduction of Model Oxides

The reduction of oxides plays a prominent role in heterogeneous catalysis. First, reducibility is important for oxidation reactions following the Mars–van Krevelen mechanism [101–103], in which mobile lattice oxygen takes part in the oxidation of reactants. In this case, the reducibility of the oxide catalyst is of key importance for the reaction process because it determines the tendency of the oxide to lose oxygen or donate it to reactants. Second, the oxide reduction can be an activation stage of the Fischer–Tropsch synthesis (FTS) [104–106], water–gas shift reaction [107,108], and dehydrogenation of hydrocarbons [109,110]. The activation, in this case, is a transformation of the catalyst from an oxidized state to an active metallic state, and the form and properties of active states can be changed drastically depending on the reductive conditions. Third, under reductive conditions, it is possible to create unique types of active states of catalysts due to nanoparticle exsolution onto the surface of mixed oxides [111,112].

In situ XRD is most often applied to the study of the process of the activation of catalysts (most commonly under reducing conditions) compared to other stages of catalyst formation or operation. This is due to the fact that during activation, the temperature and gas environment lead to changes in the oxidation state of the metal cation, resulting in the formation of intermediate states, evolution of phase composition, defect aggregation, and creation of superstructure. In situ XRD was widely applied to study the structure characteristics of catalysts during the activation process of Co-, Fe-, Cu-, and Ni-containing catalysts in a reducing atmosphere ( $\text{H}_2$ , CO, and other reducing agents). As a rule, the reducibility of reference oxides, such as  $\text{CuO}/\text{Cu}_2\text{O}$ ,  $\text{NiO}$ ,  $\text{Co}_3\text{O}_4/\text{CoO}$ ,  $\text{Fe}_2\text{O}_4$ ,  $\text{CuFe}_2\text{O}_4$ , and  $\text{CoAl}_2\text{O}_4$ , and  $\text{CeO}_2$ - and  $\text{ZrO}_2$ -based oxides, is investigated (see Figure 4).

**Reducibility of Cu-containing catalysts.** Fundamental knowledge of the kinetics and mechanism of the reduction of  $\text{CuO}$  and/or  $\text{Cu}_2\text{O}$  in  $\text{H}_2$  gas mixtures is of particular interest for heterogeneous catalysis [113], and these were thoroughly investigated by in situ XRD, TPR, and other techniques. Three different phase transformation sequences for the reduction of  $\text{CuO}$  in  $\text{H}_2$  have been reported: (1) the complete full transformation sequence  $\text{CuO} \rightarrow \text{Cu}_4\text{O}_3 \rightarrow \text{Cu}_2\text{O} \rightarrow \text{Cu}$  has only been observed for the reduction of  $\text{CuO}$  in a low-temperature hydrogen plasma [114]; (2) the direct  $\text{CuO} \rightarrow \text{Cu}$  transformation (without the formation of intermediate  $\text{Cu}_2\text{O}$  or  $\text{Cu}_4\text{O}_3$  phases) [115,116]; and (3) the sequential reduction  $\text{CuO} \rightarrow \text{Cu}_2\text{O} \rightarrow \text{Cu}$  has been reported in papers [117,118]. The reduction pathway for  $\text{CuO}$  bulk powders depends on the abundance of the reducing agent ( $\text{H}_2$  or CO): the direct  $\text{CuO}$  to  $\text{Cu}^0$  is observed for the large reactant supply, and the  $\text{CuO} \rightarrow \text{Cu}_2\text{O} \rightarrow \text{Cu}^0$  reduction—in the case of limited supply [115,119].

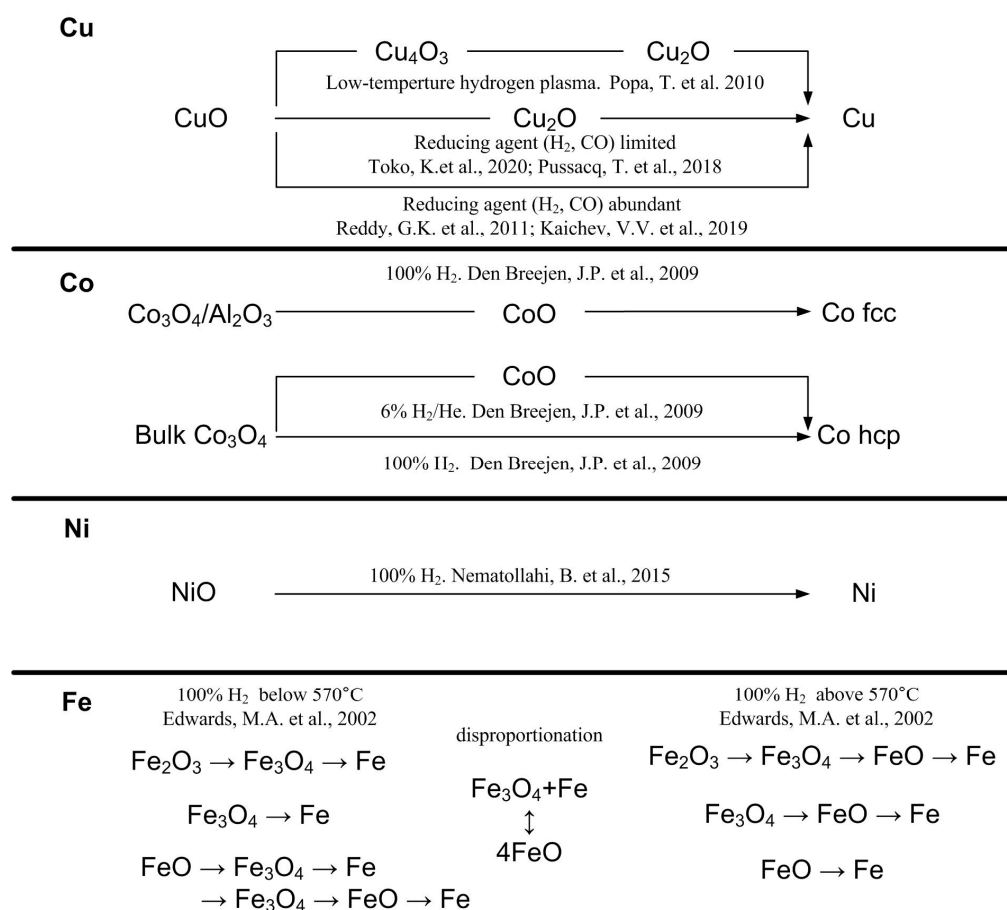


**Figure 4.** Reduction pathways for Cu, Co, Ni, and Fe oxides [107–111,120–122].

For the supported CuO/Al<sub>2</sub>O<sub>3</sub>-CeO<sub>2</sub> catalyst, the reduction of CuO to Cu<sup>0</sup> in the mixture of 5% H<sub>2</sub> and 95% N<sub>2</sub> goes both with and without the formation of intermediate states of Cu<sub>2</sub>O depending on the temperature of the catalyst preparation [123]. For the supported CuO/SiO<sub>2</sub> catalysts, one-step reduction to metal is shown regardless of preparation method (impregnation, ion exchange, deposition precipitation, urea hydrolysis-induced homogeneous deposition precipitation, and homogeneous precipitation induced by ammonia evaporation); however, the different dispersity of the resulting metal Cu is observed [124]. For the CuO/Al<sub>2</sub>O<sub>3</sub> catalyst, initially, copper is both in the form of a simple oxide of CuO and a mixed oxide of CuAl<sub>2</sub>O<sub>4</sub> with a spinel structure. It was found that copper is more easily reduced from a simple oxide than from a mixed one [125]. Plyasova et al. [126] investigated the reduction of copper from copper-containing spinels CuFe<sub>2</sub>O<sub>4</sub> and CuFeCrO<sub>4</sub> with hydrogen (5% H<sub>2</sub>/He). The mixed oxide is found to be reduced to Cu and Fe<sub>3</sub>O<sub>4</sub>. Upon mild reoxidation (270 °C, 1% O<sub>2</sub>/He), Cu<sup>0</sup> atoms partially return to the spinel structure and partially form the Cu<sub>2</sub>O or CuO phase. In addition, the authors of [127] have found that after heating mixtures of CuFe<sub>2</sub>O<sub>4</sub> with CuO in the presence of CO or CO/H<sub>2</sub>O, the copper migrates from CuO into octahedral sites of the CuFe<sub>2</sub>O<sub>4</sub> lattice at temperatures of 200–250 °C, forming metastable phase. Above 250 °C, copper leaves the oxide, the occupancy of the octahedral sites in CuFe<sub>2</sub>O<sub>4</sub> decreases, and diffraction lines for metallic Cu appear. Similar behavior of Cu atoms was detected for Ce<sub>1-x</sub>Cu<sub>x</sub>O<sub>2</sub> mixed oxide with fluorite structure [128]. Wang et al. [128] have shown that the fraction of copper that could be reduced by H<sub>2</sub> in the Ce<sub>1-x</sub>Cu<sub>x</sub>O<sub>2</sub> oxides depends strongly on the reaction temperature. A comparison with data for the reduction of pure copper oxides indicates that the copper embedded in ceria was much more difficult to reduce. The reduction of the Ce<sub>1-x</sub>Cu<sub>x</sub>O<sub>2</sub> nanoparticles was rather reversible, without the generation of a significant amount of CuO or Cu<sub>2</sub>O phases during reoxidation.

**Reducibility of Co-containing catalysts.** Supported Co-containing catalysts are of interest as FTS catalysts that are selective for the formation of normal alkanes. The precursor of the active component of the catalyst is a cobalt oxide  $\text{Co}_3\text{O}_4$ . During activation in the reductive atmosphere, Co oxides undergo a transition into the metallic state with fcc/hcp (face-centered cubic/hexagonal close packing) structure. The optimal size of metallic cobalt particles providing maximum activity and selectivity of a catalyst in the process was found to be in a range from 5 to 10 nm [120,129–132]. The performance of the active metal phase also depends on the reduction conditions. Another way to improve the selectivity and activity of the catalyst in the FTS process is an introduction of additives, such as Pt [133], Ru [134], Pd [135], Re [135], Zr [136], and other transition metals [137]. Modifications affect the properties of the initial catalyst, the process of its activation, and, accordingly, the state and structure of the active component.

In situ XRD was applied to compare the reducibility of bulk  $\text{Co}_3\text{O}_4$  with different crystal sizes and supported  $\text{Co}_3\text{O}_4/\text{Al}_2\text{O}_3$  [138]. In 100%  $\text{H}_2$ , the reduction of bulk  $\text{Co}_3\text{O}_4$  to Co with hcp structure occurs in one stage without the formation of intermediate  $\text{CoO}$ . The crystallite size of the initial  $\text{Co}_3\text{O}_4$  oxide (in the range of 14–33 nm) does not affect the temperature of reduction in this case. In 6%  $\text{H}_2/\text{He}$ , the reduction of bulk  $\text{Co}_3\text{O}_4$  (the same as for the  $\text{Co}_3\text{O}_4/\text{Al}_2\text{O}_3$  catalyst in 100%  $\text{H}_2$ ) happens in two steps,  $\text{Co}_3\text{O}_4 \rightarrow \text{CoO} \rightarrow \text{Co}$ , differing in the resulting structure of metal Co (hcp vs. fcc, accordingly). Heating of  $\text{Co}_3\text{O}_4/\text{SiO}_2$  catalysts under an inert atmosphere resulted in a selective transformation of  $\text{Co}_3\text{O}_4$  to  $\text{CoO}$  phase at 250–300 °C. The reducibility of  $\text{Co}_3\text{O}_4/\text{SiO}_2$  in hydrogen is shown to depend on the size of crystallites. The ease and completeness of reduction are found to decrease from larger (20–70 nm) to smaller particles (6 nm) [139].

Zhang et al. [140] compared the behavior of two  $\text{Co}_3\text{O}_4\text{-Al}_2\text{O}_3$  catalysts with different aluminum content and showed that aluminum interacts with cobalt oxide, preventing reduction at lower temperatures. Cherepanova et al. [141] investigated Al-modified oxides  $\text{Co}_{3-x}\text{Al}_x\text{O}_4$  with  $x = 0\text{--}0.2$ . An increase in Al ions content leads to stabilization of the intermediate  $\text{CoO}$  state during the reduction and promotes the formation of the high-temperature fcc modification of metallic cobalt. Wang et al. [142] studied modified Co-Al spinel oxide supported on the ordered mesoporous alumina. Their results obtained by in situ XRD show that the cobalt is more likely to form hcp rather than fcc structures. The other group [143] has shown that the structure of metallic cobalt (fraction of fcc and hcp modifications) obtained after reduction could be controlled by the pretreatment of carbon nanotube support.

The influence of Mn ions on the reduction of  $\text{Co}_{3-x}\text{Mn}_x\text{O}_4$  was investigated in an isothermal and temperature-programmed regime [144,145]. Two steps of subsequent reduction first include the transformation of the oxide  $(\text{Mn},\text{Co})_3\text{O}_4$  to  $(\text{Mn},\text{Co})\text{O}$ , and at the second stage, the solid solutions  $(\text{Mn},\text{Co})\text{O}$  are reduced to metallic cobalt and  $\text{MnO}$ . The introduction of manganese into the structure of cobalt oxide leads to an increase in the temperature of reduction for both stages. The structures of initial  $(\text{Mn},\text{Co})_3\text{O}_4$  and intermediate  $(\text{Mn},\text{Co})\text{O}$  oxides are very close since both spinel and rock salt structures are formed by a cubic, closely packed arrangement of oxygen. In  $(\text{Mn},\text{Co})_3\text{O}_4$ , spinel structure cations are located in octahedral and tetrahedral positions, while some of the non-spinel octahedral and tetrahedral sites remain empty. In  $(\text{Mn},\text{Co})\text{O}$ , the rock salt structure cations are located in all octahedral voids. Conversion from one to another requires only a small displacement of cations. In contrast, the formation of metallic cobalt from  $(\text{Mn},\text{Co})\text{O}$  requires rearrangement of the entire structure, which makes the effect of manganese cations on the second stage of reduction much more significant.

The authors of [146] applied the in situ XRD technique to provide insights into the formation of active phases in monometallic and bimetallic Cu–Co catalysts. The addition of Cu leads to a decrease in the reduction temperature of oxides. It is also shown that the dispersion and distribution of the Cu and Co metal onto the mesoporous matrix depends on the Cu/Co ratio. [147]. The addition of Ru accelerates the reduction of the Co oxide supported in alumina [148] and carbon nanotubes [149]. The studies of supported

Co/MWCNT (multi-wall carbon nanotubes) have shown that crystallite size, broadness of size distribution, and resistance to sintering could be controlled depending on the type of MWCNT (with a different outer diameter and wall number) and pretreatment conditions [150,151].

**Reducibility of Ni-containing catalysts.** Nickel oxide is a component in many oxidation catalysts and, in addition, is able to catalyze the methanation of CO and CO<sub>2</sub> and steam reforming [121,152–155]. Thus, the study of the reduction of this oxide is interesting not only due to its catalytic properties but also because of possible applications in the fabrication of electromagnetic devices [156,157]. The results of in situ XRD and NEXAFS/EXAFS study of the NiO reduction in the flow of hydrogen show a direct NiO → Ni transformation without the appearance of any intermediate phase. During the induction period, surface defects are formed with a high efficiency for the dissociation of hydrogen. The most common surface of the NiO is (100), and its reactivity in a non-defect state toward hydrogen is negligible. The adsorbed hydrogen has a higher adsorption energy and lower energy barrier of H–H bond breaking in the presence of oxygen vacancies, and it also can cause migration of the latter from the bulk to the surface. This shows the important role of oxygen vacancies in the nickel oxide reduction mechanism [158].

Borges et al. [159] investigated the effect of silica molar content on the performance of supported Ni/CeO<sub>2</sub>-SiO<sub>2</sub> catalyst for the steam reforming of propane. The in situ XRD data obtained in a 5% H<sub>2</sub>/He atmosphere showed that a higher silica molar content in the support contributes to an increase in the surface area and diminishes the sintering effect on ceria and nickel particles. Shimoda et al. [160] showed for the Ni- and Co-based catalysts supported on the  $\alpha$ -alumina, the formation of the Ni-Co alloy during reduction in hydrogen with a higher dispersion state compared to the single metal catalysts. Theofanidis et al. [161] investigated the reduction in H<sub>2</sub> of Ni-Rh catalyst supported on MgAl<sub>2</sub>O<sub>4</sub> and further tested the stability of the Rh-rich nickel alloy in the presence of oxidizing agents during CO<sub>2</sub>-TPO. Rh-Ni alloy forming on the surface of the catalyst suppresses H<sub>2</sub>S dissociation compared to the pure Ni catalysts and, thus, Rh enrichment increases the catalyst's resistance to the sulfur impurities in the process of dry reforming of methane. Fedorov et al. [162] investigated the influence of Cu addition on the mechanism of Ni oxide reducibility and showed a significant decrease in the activation energy of the reduction process associated with the formation of the solid solution of Cu<sup>2+</sup> in NiO. The promoting effect of Zn, Mo, and Cu in high-loading Ni-SiO<sub>2</sub> catalysts for bio-oil upgrading was studied. The introduction of additives changes the structure of metallic active components, leading to the formation of Ni<sub>1-x</sub>M<sub>x</sub> (M=Zn, Mo, Ni) solid solutions [163–168].

In the case of mixed oxide catalysts, in situ XRD is often applied to study the nickel reduction from mixed compounds such as Ni-containing layered double hydroxides [169,170], Ni-bearing clay minerals [171], Ni nanoparticles evolution from La<sub>1-x</sub>Ce<sub>x</sub>Ni<sub>1-y</sub>Al<sub>y</sub>O<sub>3</sub> perovskites [172], Ni-doped (La,Sr)FeO<sub>3</sub> [173], and (Ce,Zr)<sub>1-x</sub>Ni<sub>x</sub>O<sub>2</sub> [174,175]. Under the reductive condition, Ni cations can be released from the volume of mixed oxide with the formation of metallic Ni nanoparticles. In this case, the parent compound acts as a support and/or promoter in stabilizing Ni nanoparticles and preventing its sintering.

Marinho et al. [174] investigated the reduction of Ni for CeO<sub>2</sub> (Ni-CeO<sub>2</sub>) and CeZrO<sub>2</sub> (Ni-CeZrO<sub>2</sub>) synthesized by the sol-gel method and compared with Ni/CeO<sub>2</sub> and Ni-CeZrO<sub>2</sub> catalysts prepared by support impregnation. They found that Ni nanoparticles were embedded in the oxide after synthesis. This positively affected its sintering resistance during reduction at high temperatures (800 °C) and also led to the increased concentration of oxygen vacancies in the support.

**Reducibility of Fe-containing catalysts.** Fe-based catalysts have been the subject of intense research in recent decades due to their wide application in various fields, including water–gas shift (WGS) reactions [122,127,176,177], the Fisher-Tropsh synthesis [178], deep oxidation of CO and hydrocarbons [179], partial oxidation of H<sub>2</sub>S [180], and ammonia synthesis [181]. Indeed, the reactants in all the above-mentioned catalytic processes contain reducing agents such as CO, H<sub>2</sub>, or hydrocarbons; thus, the phase composition and the

chemical state of the Fe-based catalysts may be changed significantly under reaction conditions. From this point of view, the *in situ* XRD investigation of the reduction of iron oxides provides valuable information of practical interest.

Jozwiak et al. [182] applied *in situ* XRD to study the reduction of different oxides. Authors postulated the three-stage mechanism of reduction of hematite  $3\text{Fe}_2\text{O}_3 \rightarrow 2\text{Fe}_3\text{O}_4 \rightarrow 6\text{FeO} \rightarrow 6\text{Fe}$ , instead of the commonly accepted two-stage  $3\alpha\text{-Fe}_2\text{O}_3 \rightarrow 2\text{Fe}_3\text{O}_4 \rightarrow 6\text{Fe}$ . *In situ* XRD data indicates the appearance of the wüstite FeO phase as an intermediate of the  $\text{Fe}_3\text{O}_4$  hematite reduction process when the reaction temperature exceeds 570 °C. This happens due to the disproportionation reaction  $4\text{FeO} \leftrightarrow \text{Fe}_3\text{O}_4 + \text{Fe}$  shifting towards FeO at higher temperatures. Although this reaction is independent of the atmosphere (reducing or inert), a hydrogen environment can influence the reduction mechanism of iron oxides. At lower temperatures, the process of FeO reduction can proceed via two possible parallel pathways  $\text{FeO} \rightarrow \text{Fe}_3\text{O}_4 \rightarrow \text{Fe}$  or  $\text{FeO} \rightarrow \text{Fe}_3\text{O}_4 \rightarrow \text{FeO} \rightarrow \text{Fe}$ . Apart from reductive conditions, such as temperature, time, and pressure of the reducing agent, the particle size, crystallinity, and interaction with support play an important role.

Nielsen et al. [183] used *in situ* XRD to study the reduction and carburization processes during the activation of  $\text{Fe}_2\text{O}_3$  hematite as an FTS catalyst. It was shown that the reduction rate increases both with the temperature and hydrogen partial pressure. Moreover, the ratio of water to hydrogen determines whether the reduction path will be a two-step or a three-step process. Zheng et al. [184] have presented an *in situ* XRD investigation of the temperature-programmed reduction processes in the mixed gas ( $\text{N}_2:\text{H}_2 = 1:3$ ) of two types of industrial ammonia-synthesis catalysts ( $\text{Fe}_{1-x}\text{O}$ -based and  $\text{Fe}_3\text{O}_4$ -based). For both catalysts, the active phase  $\alpha\text{-Fe}$  is formed directly from the reduction of the precursor,  $\text{Fe}_{1-x}\text{O}$  wustite or  $\text{Fe}_3\text{O}_4$  magnetite, and no other intermediate phases were observed. The  $\text{Fe}_{1-x}\text{O}$ -based catalyst has been shown to have a lower reduction temperature and a faster reduction rate than the  $\text{Fe}_3\text{O}_4$ -based catalyst. The authors also stated that the higher value of lattice microstrain of the active phase  $\alpha\text{-Fe}$  obtained from  $\text{Fe}_{1-x}\text{O}$ -based catalyst is one of the other possible origins of the difference in the catalytic activity between the two catalysts.

The introduction of additives can lead to the formation of mixed oxides, the reduction mechanism of which is different from that for simple oxides. The addition of Cr [108], Ce [185], and Al [185] to hematite increases the transformation temperature of  $\text{Fe}_2\text{O}_3$  to  $\text{Fe}_3\text{O}_4$ , whereas the addition of Au [186] and Cu [185] leads to a decrease in the reduction temperature. Zhao and co-workers [187] found that doping with Ca increases the reduction rate of  $\text{Fe}_2\text{O}_3$ ; the greatest effect is observed for the phase transition of FeO to metallic iron. Addition of Cu significantly decreases the reduction temperature of hematite to magnetite ( $\text{Fe}_2\text{O}_3 \rightarrow \text{Fe}_3\text{O}_4$ ) [185]. Shi et al. [188] studied the structure evolution of bimetallic  $\text{Fe m}$  ( $\text{M}=\text{Fe, Mn, Co, Ni}$ ) ferrite spinel in a flow of 3%  $\text{H}_2$  in Ar by *in situ* XRD. The results revealed that the doping by a second metal decreases the crystallite and particle sizes. Also, the doping by Mn promotes the reduction of the  $\text{Mn}_x\text{Fe}_{3-x}\text{O}_4$  phase to the  $\text{Mn}_x\text{Fe}_{1-x}\text{O}$  phase; however, further reduction of  $\text{Fe}^{2+}$  in the  $\text{Mn}_x\text{Fe}_{1-x}\text{O}$  phase is inhibited, while the doping by Co and Ni favors the reduction of  $\text{M}_x\text{Fe}_{3-x}\text{O}_4$  to alloy and metal phases.

The effect of potassium promoter on phase transformation during reduction of the Fe-based catalysts was investigated by *in situ* XRD [189–191]. The reduction pathway of  $\alpha\text{-Fe}_2\text{O}_3$  follows the two-step sequence of  $\alpha\text{-Fe}_2\text{O}_3 \rightarrow \text{Fe}_3\text{O}_4 \rightarrow \alpha\text{-Fe}$  during the isothermal treatment in 10%  $\text{H}_2/\text{He}$  in contrast to that of  $\alpha\text{-Fe}_2\text{O}_3 \rightarrow \text{Fe}_3\text{O}_4 \rightarrow \text{FeO}/\alpha\text{-Fe} \rightarrow \alpha\text{-Fe}$  during the temperature-programmed reduction [189]. The potassium promoter inhibits the reduction of  $\alpha\text{-Fe}_2\text{O}_3$  to  $\text{Fe}_3\text{O}_4$  due to the enhanced strength of Fe-O bonds while enhancing the transition from  $\text{Fe}_3\text{O}_4$  to  $\alpha\text{-Fe}$ . Zhang et al. [190] investigated the reducibility of  $\text{Fe}_3\text{O}_4$  for supported  $\text{FeK}/\text{Al}_2\text{O}_3$  and  $\text{FeK}/\text{M-Al}_2\text{O}_3$  ( $\text{M}=\text{Ce, Y and La}$ ) catalysts of  $\text{CO}_2$  hydrogenation. The results indicated that the addition of rare earth metals is beneficial for the transition from  $\text{Fe}_3\text{O}_4$  to  $\text{FeO}$  process, which is an important step for further formation of the catalytically active iron carbide. Yang et al. [191] have found for  $\text{K-Cu-Fe/SiO}_2$  catalysts of FTS that  $\alpha\text{-Fe}_2\text{O}_3$  is also transformed via sequence  $\text{Fe}_2\text{O}_3 \rightarrow \text{Fe}_3\text{O}_4 \rightarrow \text{FeO} \rightarrow \text{Fe}$  and further to  $\text{Fe}_2\text{C}$  iron carbide during the CO reduction process.

The authors of [192,193] investigated the influence of Cu and Al additives on the reduction of iron oxides in CO. Al inhibits both reduction rates for the  $\text{Fe}_2\text{O}_3 \rightarrow \text{Fe}_3\text{O}_4$  and  $\text{Fe}_3\text{O}_4 \rightarrow \text{FeO}$  transformations. In situ XRD results show that the Al modifications stabilize the small particle size of intermediate  $\text{Fe}_3\text{O}_4$  oxide and prevent its further sintering due to the formation of  $\text{Fe}_{3-x}\text{Al}_x\text{O}_4$  solid solution. The introduction of copper to the Al-modified  $\text{Fe}_3\text{O}_4$ - leads to the formation of highly dispersed  $\text{CuO}$  particles over the catalyst surface and mixed oxide  $\text{CuFe}_2\text{O}_4$ . The reduction of Cu oxides to metal state accelerates the  $\text{Fe}_2\text{O}_3 \rightarrow \text{Fe}_3\text{O}_4$  and  $\text{FeO} \rightarrow \text{Fe}$  transformations but does not affect the  $\text{Fe}_3\text{O}_4 \rightarrow \text{FeO}/\text{Fe}$  stages.

**Reducibility of  $\text{CeO}_2$ -based catalysts.** Redox behavior in  $\text{CeO}_2$ -containing oxide catalysts is widely investigated by in situ XRD as a reference compound in the context of application in three-way catalysts for exhaust gas control and solid oxide fuel cell (SOFC) and solid oxide electrolyzer cell (SOEC) construction [194–198]. Structural effects of hydrogen dissolution and oxygen extraction, and also the structural stability of crystalline ceria phases in undoped and doped ceria-based materials by various elements, including Sm [195], Zr [174,175], Ni [174,175,199,200], Cu [200,201], Mn [202], Fe [200], and Co [203,204], were studied. In the case of  $\text{CeO}_2$ -based catalysts, in situ XRD is often applied to monitor the evolution of the oxide lattice parameter as a function of the temperature and gas composition because a comparison of lattice parameters' behavior for the ceria-based catalyst and pure ceria illustrates the processes of cation evolution from the solid solution, reducibility of oxide, and formation of oxygen vacancies in the ceria structure. Zhang et al. [200,204] followed changes in the ceria lattice parameter as a function of temperature in the  $\text{MO}_x/\text{CeO}_2$  ( $\text{M}=\text{Cu}, \text{Ni}, \text{Co}, \text{Fe}$ ) sample during the  $\text{CH}_4$ -TPR reaction and showed that the onset temperature of the apparent ceria reduction manifested varies slightly following an order of  $\text{CuO}_x/\text{CeO}_2 < \text{NiO}_x/\text{CeO}_2 < \text{CoO}_x/\text{CeO}_2 < \text{FeO}_x/\text{CeO}_2$ . In the case of the  $\text{Ce}_{0.8}\text{Cu}_{0.2}\text{O}_2$  catalyst, the change in the ceria lattice parameter indicates that the reduction and oxidation of Cu and Ce in a solid solution is reversible [128].

Zhang et al. [175] found that ceria-zirconia-supported Ni ( $\text{Ni}/\text{CeZrO}_2$ ) is of higher reducibility than the pure ceria-supported Ni ( $\text{Ni}/\text{CeO}_2$ ) upon reaction with pure  $\text{CH}_4$  or for the methane dry reforming (DRM) reaction. Zr in the ceria support prevents particle sintering and maintains small particle sizes for both metallic nickel and the partially reduced ceria support under reaction conditions through a stronger metal-support interaction. Additionally, Zr prevents Ni migration from the surface into ceria, forming a  $\text{Ce}_{1-x}\text{Ni}_x\text{O}_{2-y}$  solid solution, which is seen in  $\text{Ni}/\text{CeO}_2$ , thus helping to preserve the active  $\text{Ni}^0$  on the  $\text{Ni}/\text{CeZrO}_2$  surface. Marinho et al. [174] have shown that doping of ceria with Zr helps to maintain the ceria structure during thermal treatment for similar systems. It also increases the mobility of lattice oxygen compared to ceria alone and suppresses carbon deposition during the DRM.

### 3.3. Study of the Catalyst under Reaction Conditions (Operando)

Under reaction conditions, a catalyst may undergo chemical transformations that drastically modify its bulk and surface properties. To elucidate how the reactants, intermediates, and products of the catalytic process change the active phase composition and structure, a combination of an in situ XRD technique and analysis of the gas phase is necessary. On-line monitoring of the gas phase is usually performed by either mass spectrometry or fast gas chromatography. In order to obtain a full picture of the catalytic process, in situ techniques, which focus on the bulk characterization of the catalyst, such as XRD and XAFS, and other techniques, such as NAP-XPS and IR spectroscopy, that are better suited for studying the surface chemistry associated with the reaction process, should be used. However, in some cases, the use of in situ XRD analysis alone or in combination with analysis of the gas phase is sufficient to provide valuable information on catalyst performance.

Typically, operando XRD is applied to elucidate the structure of active component under conditions of several processes: methane dry reforming ( $\text{CH}_4 + \text{CO}_2 \rightarrow \text{CO} + \text{H}_2$ ) [175,204–208], methanol/ethanol steam reforming ( $\text{CH}_3\text{OH} + \text{H}_2\text{O} \rightarrow \text{CO}_2 + 3\text{H}_2$ ,  $\text{C}_2\text{H}_5\text{OH} + \text{H}_2\text{O} \rightarrow 2\text{CO}_2 + 4\text{H}_2$ ) [209,210], the water-gas shift (WGS,  $\text{CO} + \text{H}_2\text{O} \rightarrow \text{H}_2 + \text{CO}_2$ ) [211,212], and the partial oxidation of hydrocarbons ( $\text{C}_2\text{H}_6 + \text{O}_2 \rightarrow \text{CO}_2 + \text{H}_2\text{O}$ ) [213,214].

$\text{CO}_2$ ) [176,201,211–216], the reverse water–gas shift reaction (RWGS,  $\text{H}_2 + \text{CO}_2 \rightarrow \text{CO} + \text{H}_2\text{O}$ ) [217–219], total oxidation reactions of CO and hydrocarbons, catalytic hydrogenation and dehydrogenation [220–224], and self-sustained reaction-rate oscillations ( $\text{CO} + \text{O}_2 \rightarrow \text{CO}_2, \text{CH}_4 + \text{O}_2 \rightarrow \text{CO}_2 + \text{H}_2\text{O}$ ) [51,102,225–229]. In all the above-mentioned applications, the phase composition and the chemical state of the catalysts are strongly dependent on the reagent/product composition in a certain reaction process. For example, in the case of oxidation reactions, the state of the catalyst is determined by the fuel (CO,  $\text{H}_2$ , hydrocarbons)-rich or -lean conditions. Under the fuel-rich condition, the more reducing environment promotes the formation of metal phases or stable oxides, while under the fuel-lean condition, oxygen-rich compounds are formed.

**Methane dry reforming, methanol/ethanol steam reforming.** The conversion of methane, as the main constituent of natural gas and biogas, to higher-value products has received much attention in recent years, especially the reforming process of methane to syngas, which can be used as a fuel or an intermediate in the production of other chemicals [230,231]. Dry methane reforming (DRM,  $\text{CH}_4 + \text{CO}_2 \rightarrow \text{CO} + \text{H}_2$ ) is a high-value-added energy conversion process due to its low operating cost and utilization of  $\text{CH}_4$  and  $\text{CO}_2$ , which are both high-impact greenhouse gases [232,233]. Moreover, the syngas produced by DRM have a  $\text{H}_2:\text{CO}$  ratio of 1:1, which is preferred for the formation of oxygenated chemicals and liquid hydrocarbons through the Fischer–Tropsch synthesis. Different metal catalysts have been successfully applied to catalyze the DRM reaction. For this type of catalytic reaction, operando XRD is applied to determine the state of the catalyst under operating conditions since reactants  $\text{CH}_4$  and  $\text{CO}_2$  can interact with the catalyst and change its active state [204–206]. Wang et al. [205] show the structural transition of the alloy in Ni-catalyst supported on hierarchical Fe-modified  $\text{MgAl}_2\text{O}_4$  in different reactive environments of methane dry reforming (ratio  $\text{CH}_4:\text{CO}_2$ ). It has been found that the activity of the catalyst and the resistance to carbon deposition are strongly dependent on the Ni/Fe ratio used. The most active Ni–Fe surface alloy is formed at the ratio  $\text{Fe}/\text{Ni} \leq 0.1$ , and an excess of Fe leads to catalyst deactivation. Zhang et al. [204] studied a series of Co-loaded  $\text{CeO}_2$  catalysts in the DRM process. According to an in situ XRD study, a strong interaction of methane with the  $\text{CoO}_x\text{--CeO}_2$  systems at temperatures in the range 200–350 °C occurs. The hydrogen produced by the dissociation of C–H bonds in methane leads to a full reduction of Co oxide to metallic state,  $\text{Co}_3\text{O}_4 \rightarrow \text{CoO} \rightarrow \text{Co}$ , and a partial reduction of ceria. Both XRD and AP-XPS have shown that under optimum reaction conditions, the active phase contains metallic Co with a small amount of CoO, both supported on a partially reduced ceria. The authors of [234] monitored the in situ formation of a graphitic surface carbon on the 5% Ni/MnO catalyst and the growth of nickel particles during DRM. The comparison between the catalytic tests and the in situ XRD data suggests that surface carbon produced during DRM over the 5% Ni/MnO catalyst does not lead to catalyst deactivation but can act as a reaction intermediate for dry reforming of methane. Marin et al. [206] conducted an in situ XRD study of the strontium-doped lanthanum cobaltite (LSC) microwave catalyst promoted with Mn to control the catalyst oxophilicity during thermal DRM. The experimental results proved that metallic Co particles are an active component of the LSC-Mn catalyst in the DRM reaction but not  $\text{La}_2\text{O}_3$ , as was implied earlier. The authors also demonstrated that the catalyst can be regenerated under oxidizing conditions and fully restores the initial structure.

Liu et al. [209] investigated the methanol steam reforming reaction  $\text{CH}_3\text{OH} + \text{H}_2\text{O} \rightarrow \text{CO}_2 + 3\text{H}_2$  on a Ni- $\text{CeO}_2$  catalyst. Both surface  $\text{NiO} \rightarrow \text{NiC} \rightarrow \text{Ni}$  and bulk  $\text{CeO}_2 \rightarrow \text{CeO}_{2-x}$  phase transitions were observed during the reaction. The authors demonstrated that metallic nickel supported over  $\text{Ce}^{3+}$ -rich ceria is the active phase of the Ni- $\text{CeO}_2$  catalyst. They also showed, via modeling of the methanol reaction on the Ni- $\text{CeO}_{2-x}$  (111) plane, that metal–support interactions in this system are crucial to the high selectivity for  $\text{CO}_2$  vs.  $\text{C}_{\text{surf}}/\text{CO}$  production. Zhou et al. [210] compared the structure characteristics of  $\text{Ce}_{0.8}\text{Ni}_{0.2}\text{O}_2$  and  $\text{Ni}_{10}/\text{CeO}_2$  catalysts (with the same mole fraction of Ni) under ethanol steam reforming. For both catalysts, a  $\text{NiO} \rightarrow \text{Ni}$  transformation at temperatures above

400 °C was observed. However, XRD data showed that the lattice of ceria cells changed differently. Lattice expansion in  $\text{Ce}_{0.8}\text{Ni}_{0.2}\text{O}_2$  was 1.5 times larger than in  $\text{Ni}_{10}/\text{CeO}_2$ , indicating the substantially larger number of oxygen vacancies in  $\text{Ce}_{0.8}\text{Ni}_{0.2}\text{O}_2$  oxide. The study showed that nanoparticles of nickel were embedded into the ceria lattice during the reaction. This suppressed the methanation activity and induced the formation of additional oxygen vacancies in the oxide, enhancing the breaking of O-H bonds for both water and ethanol.

**The water–gas shift and reverse water–gas shift reactions.** In 2013, Rodrigues and colleagues [176] published a review of *in situ/operando* studies for the production of hydrogen through the water–gas shift  $\text{CO} + \text{H}_2\text{O} \rightarrow \text{H}_2 + \text{CO}_2$  on metal oxide catalysts. The active phase of the catalysts in the WGS process requires identifying and characterizing to optimize existing or to design new effective catalysts. In most cases, a catalyst under reaction conditions undergoes transitions drastically, modifying its composition and structure with respect to those obtained during the synthesis process. Typically, one needs to use *in situ* XRD to study the structure of crystalline samples that have long-range order and XAFS or PDF to obtain information on a local structure, which is especially useful for samples that have low crystallinity or are amorphous. Experiments of time-resolved *in situ* XRD, XAFS, and PDF indicate that the active phase of the WGS catalysts, which combine Cu, Au, or Pt with oxides such as ZnO [211],  $\text{CeO}_2$  [201],  $\text{TiO}_2$ ,  $\text{CeO}_x/\text{TiO}_2$  [212], and  $\text{Fe}_2\text{O}_3$  [213], essentially involves nanoparticles of the reduced metals. It was shown for these systems that oxide support is partially reduced in the process and is involved in the dissociation of water and, in some cases, changes the chemical properties of the active metal phase. Vovchok et al. [214] investigated mesoporous Co/ $\text{CeO}_2$  catalysts for the high-temperature WGS. It was demonstrated that the reducibility of the ceria depends on the cobalt loading. The increased concentration of Co in the ceria structure suppressed the reduction of Ce cations, thereby reducing the oxygen vacancies, and likely had an adverse effect on activity. Lopez Camara et al. [215] studied the promotion effect of Mn on inverse  $\text{CeO}_2/\text{CuO}$  catalysts. The main conclusion was that the catalytic properties are determined mostly by the properties of ceria nanoparticles. It has been found that manganese suppresses the reduction of the copper oxide support to a certain extent and simultaneously increases the reducibility of ceria particles. This may contribute to the activation of water and/or the formation of active intermediates, which in turn leads to increased WGS activity. Developing techniques for catalytic  $\text{CO}_2$  reduction to make higher-value products, such as fuels or key molecular building blocks for the chemical industry, is a promising way to ameliorate this threat.  $\text{CO}_2$  hydrogenation to CO is commonly known as the reverse water–gas shift (RWGS) reaction and can be coupled with other processes, such as Fischer–Tropsch synthesis. This is one of the reasons the RWGS process continues to be extensively studied as a  $\text{CO}_2$  mitigation strategy. Wang et al. [218] investigated how a change in the structure of the  $\text{In}_2\text{O}_3$  crystal phase alters the catalytic performance in the RWGS reaction.  $\text{In}_2\text{O}_3$  with cubic lattice shows stable catalytic performance under high-temperature RWGS conditions (at 450 °C), while the hexagonal form slowly (hours) changes to the cubic. The authors suggest that the phase transition occurs due to the reduction of h- $\text{In}_2\text{O}_3$  to In(0) or  $\text{In}_2\text{O}_x$  with hydrogen, followed by the oxidation of reduced forms to c- $\text{In}_2\text{O}_3$  with  $\text{CO}_2$ . Lin et al. [219] investigated the promotion effect of  $\text{FeO}_x$  on the Cu/ $\text{CeO}_2$  catalyst in the RWGS reaction. It was shown that the CuFe/ $\text{CeO}_2$  catalyst exhibits high stability compared to the monometallic Cu/ $\text{CeO}_2$  in reaction conditions without sacrifice to activity. During activation in a reducing medium, the metallic states of iron and copper are formed. As soon as the atmosphere changes to the RWGS conditions, the dispersed FeO phase appears, while the copper phase remains intact. The authors proposed that the iron oxides (with limited loading) act as textural promoters for the copper, preventing its sintering.

Other interesting processes to study using the *operando* technique are the reaction rate oscillation reactions [51,228,229] (see Figure 5). Although this is fundamental research, it is still possible to obtain a lot of useful information, such as details about reaction mechanisms or the structure of the active phase of the catalyst, for further use in more applied research.

The authors studied the self-sustained relaxation-type oscillations in the catalytic oxidation of methane over palladium [228,229] and nickel [51].

Using XRD and MS methods, it has been shown that in an oxygen-deficient environment, oscillations of reagents and products occur, accompanied by simultaneous oscillations of temperature and phase transitions. XRD data showed that the highly active state of  $\text{Pd}^0$  periodically transforms into the low-active state of  $\text{PdO}$  in the form of a thin film on the surface. The reverse transition is accompanied by the carbon deposition on the surface and its dissolution in the Pd lattice. Similar results were obtained for nickel, where a much larger part of the catalyst was involved in the reversible Ni–NiO transitions, and no significant carbon deposition was observed.

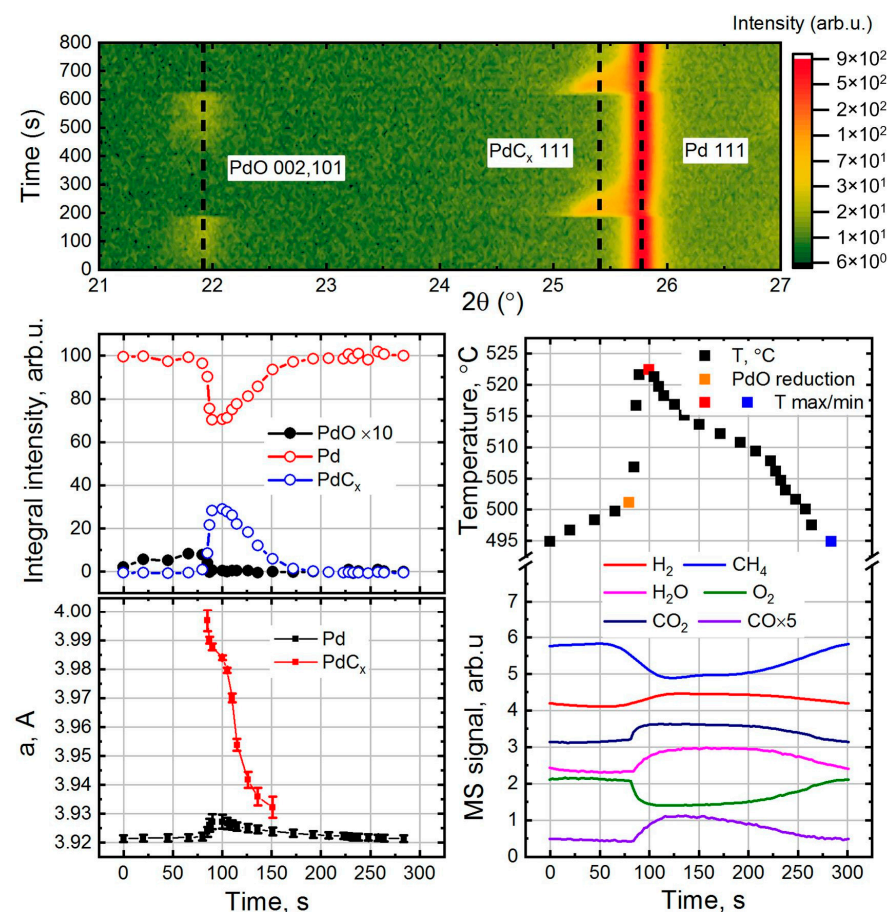


**Figure 5.** Map of diffraction intensity versus time and diffraction angle ( $\lambda 0.1 \text{ nm}$ ) obtained during the self-sustained oscillations in methane oxidation reaction over palladium (**top**). Corresponding graphs of the integral diffraction intensity for Pd,  $\text{PdC}_x$ , and  $\text{PdO}$ , as well as the lattice parameters of the Pd and  $\text{PdC}_x$  phases versus time (obtained from diffraction patterns averaged over several oscillations) (**bottom left**). Corresponding temperature and mass spectrometer signals versus time (**bottom right**). The figures are based on the data presented in [228,229].

### 3.4. Study of the Process of the Deactivation of Catalysts

The deactivation of the catalyst is an important stage in its lifetime. Understanding the nature of this process opens up opportunities to extend catalyst life and develop efficient regeneration/recycling strategies. The common types of deactivation mechanisms (see Figures 6 and 7) reported for the heterogeneous catalysts include [235] poisoning (catalytic sites blockage by a chemisorbed agent), thermal degradation (loss of the active phase or catalyst surface), fouling (physical blockage of the catalyst surface by a deposited agent), active component leaching (through a liquid or gas phase), inactive phase formation, attrition/crushing, photodegradation (due to exposure to light or radiation), and elec-

trodegradation (changes in catalyst structure due to applied voltage). Since deactivation processes can be long in time and require conditions similar to the real processes, various approximations are often used to model them. This can be a study of the catalyst resistance to overheating by a temperature treatment in various media or, for example, enrichment of the reaction media with fuel to accelerate the processes of carburization. There are comprehensive reviews [235,236] that have addressed the topic of the mechanisms of catalyst deactivation. This brief review is aimed to cover the studies that have successfully applied *in situ* XRD to the matter.

NAP-XPS, *in situ* XRD, and EXAFS were applied to study the reasons for a higher tolerance toward severe reaction conditions (high temperature and/or enhanced ethane/oxygen ratio) of the Bi-modified MoVNbTeO catalysts for oxidative dehydrogenation of ethane [237]. In earlier works, it was found that the main mechanism of the MoVNbTeO catalyst deactivation in reaction conditions is caused by the reduction of tellurium, further accompanied by either blocking of the active sites or decomposition of the initial catalyst structure. It was directly shown by *in situ* XRD that under strong reducing conditions, the crystal lattice of the bi-modified catalyst did not undergo compression along the *c*-axis, in contrast to the initial catalyst. Together with EXAFS data showing that Bi has a similar local environment as Te, this allowed the authors to state that Bi limits Te mobility within the oxide structure.

The industrial catalytic dehydrogenation of ethylbenzene accounts for ~90% of the styrene produced worldwide. Muhler et al. [220,238,239] used *in situ* XRD to elucidate the origin of activation and deactivation of a potassium-promoted iron oxide catalyst. Authors indicated that the reduction process during the start-up period causes the release of mobile K<sup>+</sup> ions, which in turn react with trivalent iron oxides to form the active phase of KFeO<sub>2</sub>. Under reaction conditions, KFeO<sub>2</sub> exists as a thin layer supported on a solid solution of K<sub>2</sub>Fe<sub>22</sub>O<sub>34</sub> in Fe<sub>3</sub>O<sub>4</sub>, but it is metastable at room temperature and in the presence of moisture. The deactivation of the catalyst may take place by complete reduction of KFeO<sub>2</sub> to Fe<sub>3</sub>O<sub>4</sub> and KOH. The formation of a liquid phase (KOH) causes the loss of potassium and irreversible deactivation of a catalyst.

Oxidative coupling of methane (OCM) is one of the chemical processes that converts methane directly into more valuable C<sub>2</sub> products. La<sub>2</sub>O<sub>3</sub>-based catalysts are promising in OCM reactions; however, under CO<sub>2</sub> (major by-product) exposure, the effect of bulk carbonation of La<sub>2</sub>O<sub>3</sub> takes place, affecting C<sub>2</sub> yield performance. Guan et al. [240] compared two La<sub>2</sub>O<sub>3</sub> samples, a commercial isotropic M-La<sub>2</sub>O<sub>3</sub> and one with optimized nanorod morphology n-La<sub>2</sub>O<sub>3</sub> in OCM reaction, while measuring XRD and MS in real time. They showed that, having the same hexagonal structure, n-La<sub>2</sub>O<sub>3</sub> is more resistant to the formation of La<sub>2</sub>O<sub>2</sub>CO<sub>3</sub> and that the latter has a poisoning effect on the activity of La<sub>2</sub>O<sub>3</sub>.

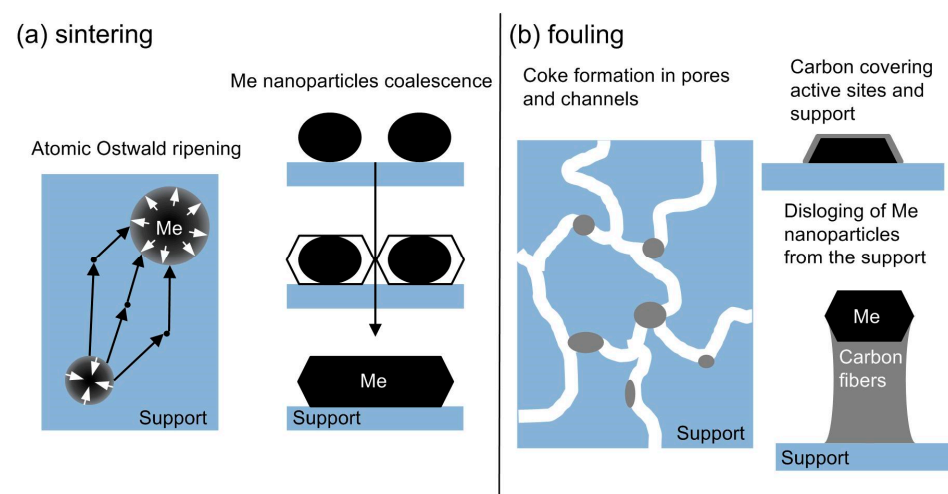


**Figure 6.** The common types of deactivation mechanisms: (a) sintering via atomic Ostwald ripening and crystallite migration; (b) catalyst surface and pores carbonization.

Currently, steam reforming of the liquefied petroleum gas (SR-LPG) process is considered an alternative to steam methane reforming (industrial technology standard) due to the safer storage and easier distribution in remote areas. Due to the decomposition of LPG and methanation reaction, a lot of hydrocarbon by-products are produced, affecting the catalysts' activity via carbon deposition. Moura et al. [241] studied the stability of Ni, Rh, Ru, and Pt catalysts supported on ceria–silica. In situ XRD data collected during the SR-LPG process established high stability to sintering of the Pt, Rh, and CeO<sub>2</sub> structures, while the crystallite sizes of Ni<sup>0</sup> and Ru<sup>0</sup> tend to increase with time in the reaction. The authors attributed this effect, i.e., decreasing the metal–support interfacial area for Ni and Ru samples, to an alternative reason for the deactivation of these catalysts, in addition to carbon deposition on the catalyst surface.

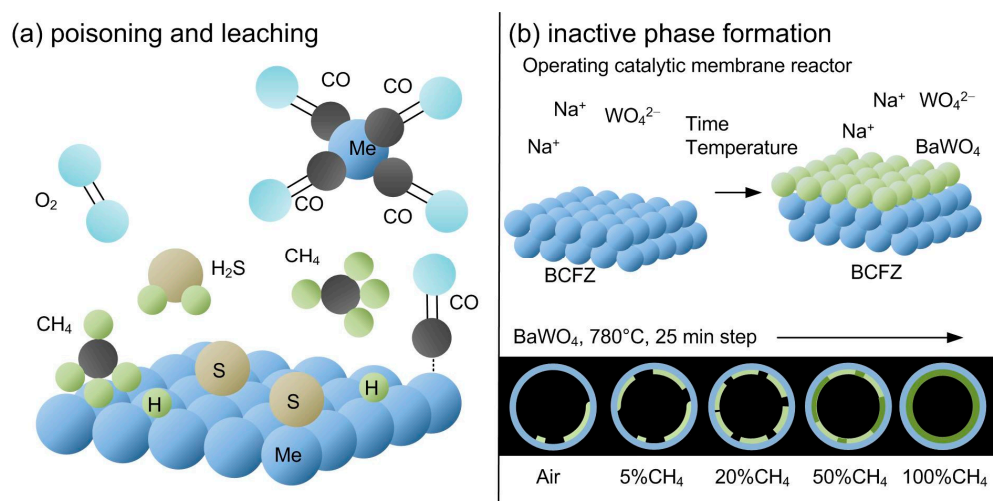


**Figure 7.** The common types of deactivation mechanisms: (a) catalyst sulfur poisoning and carbonyl leaching; (b) thermal-driven growth of the BaWO<sub>4</sub> inner layer at the BCFZ membrane blocking the oxygen transport (figure adapted from data obtained in [242]).

Sintering, typically a process of crystallite growth or agglomeration with loss of catalytic surface area, is the main reason for the loss of activity of a wide range of catalysts. When speaking about supported metal catalysts, several different parameters can affect sintering rates, including temperature; environment; metal type; catalyst dispersion; and support surface area, texture, and porosity [236]. Typically, sintering rates increase exponentially with temperature, and in most cases, this is an irreversible process. Thus, the best strategy is to mitigate or prevent the effect rather than to reverse it. In a reducing or neutral environment, generally, the melting point of the used metal determines the sintering effects, i.e., stability drops in the following order: Pt > Pd > Ni > Cu. In the oxidizing conditions, the metal oxide volatility and metal–support interactions play a crucial role; for example, for noble metals, stability drops in the following order: Rh > Pt > Ir > Ru (melting temperature order: Ru > Ir > Rh > Pt). An effective way to increase resistance to sintering is to use a support with a strong interaction with the catalyst and/or encapsulate the metal in the porous matrix. Kim et al. [243] studied Pt cluster stability during ethylene hydrogenation by operando XAS and in situ X-ray PDF analysis. The Pt clusters and single atoms were deposited on inorganic zirconia nodes of a metal–organic framework (MOF) NU-1000 using targeted vapor-phase synthesis. The authors confirmed that in reducing and operating conditions up to 200 °C, no significant changes in cluster sizes were present. They also found that single atoms of Pt are more susceptible to CO poisoning due to stronger bonding. The other way to prevent sintering is to use promoters/protectors or complex bi- or tri-metallic catalysts. It was identified that the sintering of copper in the Cu/ZnO/Al<sub>2</sub>O<sub>3</sub> catalysts is one of the deactivation mechanisms in methanol synthesis [244–246]. In situ XRD tests were conducted for Cu/ZnO/Al<sub>2</sub>O<sub>3</sub> catalyst in the

temperature range from 110 °C to 640 °C in a reduction atmosphere. It was found that the Zn promoter can efficiently prohibit the growth of Cu particles at lower temperatures. However, with the extended time and temperature exposure, the Cu particles continued to inevitably grow due to the loss of ZnO protection after its reduction [246].

Another wide area of research includes complex oxides with perovskite ( $\text{ABO}_3$ ) or perovskite-like ( $\text{A}_2\text{BO}_4$  Ruddlesden–Popper phase) and fluorite ( $\text{AO}_2$ ) structures. Typical applications of these are oxygen separation membranes, catalytic membrane reactors (CMR) for producing syngas from biofuels, and solid oxide fuel cells (SOFC). General requirements for such materials are chemical and thermomechanical stability under a high gradient of the oxygen chemical potential, high oxygen or mixed ionic–electronic conductivity and surface reactivity, high selectivity in the partial oxidation of fuels into syngas, and relatively low cost. The common deactivation mechanisms include [247] thermal degradation (phase segregation under high temperature and/or under oxygen-rich/deficient atmosphere) [248–250]; inactive phase formation or poisoning (either due to the chemical reaction between component layers for SOFC or due to the interaction with the gas phase for catalytic reactors) [242,251]; and mechanical cracking (which is often the case for layered SOFCs during thermal cycling of components with different thermal expansion coefficients (TECs)) [252,253]. Popov et al. [249] constructed a reactor for in situ XRD studies of oxygen-permeable membranes compatible with a conventional D8 Advance (Bruker) powder diffractometer. Using this setup, the authors have shown that the structure of the membrane based on the  $\text{Ba}_{0.5}\text{Sr}_{0.5}\text{Co}_{0.78}\text{W}_{0.02}\text{Fe}_{0.2}\text{O}_{3-\delta}$  under operating conditions is determined by the oxygen partial pressure from the feed side. Therefore, the popular opinion that membranes based on cobaltites are unstable is not relevant for thin-walled hollow fiber membranes. Nikolaeva et al. [251] tested a  $\text{La}_{0.5}\text{Ca}_{0.5}\text{Mn}_{0.5}\text{Co}_{0.5}\text{O}_3$  solid solution as a catalyst for the total methane combustion reaction. During the reaction, there was a noticeable decrease in methane conversion, and the rate of catalyst deactivation increased with increasing temperature. The in situ XRD and HRTEM methods showed that the deactivation occurs as a result of the segregation of calcite and cobalt oxide particles on the perovskite surface. Vamvakeros et al. [242] studied CMRs under OCM reaction conditions using XRD with absorption computed tomography (-CT) technique. They have shown that both  $\text{BaCo}_{0.4}\text{Fe}_{0.4}\text{Zr}_{0.2}\text{O}_{3-\delta}$  (BCFZ) and  $\text{La}_{0.6}\text{Sr}_{0.4}\text{Co}_{0.2}\text{Fe}_{0.8}\text{O}_{3-\delta}$  (LSCF) membranes are chemically stable in  $\text{CO}_2$  atmosphere. However, the observed formation and growth of stable  $\text{BaWO}_4$  and  $\text{SrWO}_4$  phases could lead to deactivation of the membranes due to the inner layer formation blocking the flow of oxygen and W loss by the catalyst phase. Another excellent work was carried out by Li et al. [253] using the same XRD-CT technique to study a complete micro-monolithic SOFC (composition—8 mol% YSZ, NiO, and lanthanum strontium manganite) during thermal cycling in real time. The authors demonstrated superior mechanical properties of this design, consistent chemical and structural homogeneity, and, of course, the possibility to observe these parameters with high spatial resolution in operating full cells.

#### 4. Conclusions and Outlook

In this brief review, we demonstrated different aspects of the application of in situ XRD for modern oxide and metal oxide catalysis. XRD's ability to determine the nanostructure of catalysts and phase dynamics under synthesis/activation/reaction conditions makes it a powerful tool for catalysis research. Thus, this technique should unambiguously be the basis of any catalytic research. Still, in the literature, the speculations about the state of the active phases dominate the discussions of the real data obtained under operating conditions. However, the field of in situ techniques application is growing, and it is definitely connected with progress in experimental facilities and equipment. Development in radiation sources with higher brilliance, state-of-the-art 2D detectors, reaction cells, and neural network technologies are all driving forces for in situ XRD experiments. With the increasing availability of this type of research, we are definitely seeing a shift in in situ XRD from an exclusive study to a routine one.

New directions have emerged for in situ diffraction, especially in the field of characterization by multiple techniques, such as a common tandem XRD-EXAFS. The combination of in situ/operando techniques, both bulk- and surface/element-sensitive, could provide detailed studies of the structural, electronic, and chemical properties of catalysts under reaction conditions. All the required technology is available to make it possible, and the limitations are the centralization and system integration of these techniques at the dedicated centers in institutions/synchrotron facilities.

**Author Contributions:** Writing—original draft preparation and writing—review and editing, O.A.B. and Z.S.V.; visualization, Z.S.V. All authors have read and agreed to the published version of the manuscript.

**Funding:** This work was supported by the Ministry of Science and Higher Education of the Russian Federation (Grant Agreement No. 075-15-2022-263).

**Data Availability Statement:** No new data were created or analyzed in this study. Data sharing is not applicable to this article.

**Acknowledgments:** The experiments were performed using large-scale research facilities, “EXAFS spectroscopy beamline”, at the Siberian Synchrotron and Terahertz Radiation Center.

**Conflicts of Interest:** The authors declare no conflict of interest.

## References

1. Mosesman, M.A. In Situ X-ray Diffraction Studies of Heterogeneous Reactions. *J. Am. Chem. Soc.* **1951**, *73*, 5635–5639. [[CrossRef](#)]
2. Bañares, M.A.; Wachs, I.E. Molecular Structures of Supported Metal Oxide Catalysts under Different Environments: Molecular Structures of Supported Metal Oxide Catalysts. *J. Raman Spectrosc.* **2002**, *33*, 359–380. [[CrossRef](#)]
3. Hull, A.W. A New Method of X-ray Crystal Analysis. *Phys. Rev.* **1917**, *10*, 661–696. [[CrossRef](#)]
4. Velasco-Vélez, J.J.; Teschner, D.; Girgsdies, F.; Hävecker, M.; Streibel, V.; Willinger, M.G.; Cao, J.; Lamothe, M.; Frei, E.; Wang, R.; et al. The Role of Adsorbed and Subsurface Carbon Species for the Selective Alkyne Hydrogenation over a Pd-Black Catalyst: An Operando Study of Bulk and Surface. *Top. Catal.* **2018**, *61*, 2052–2061. [[CrossRef](#)]
5. Timoshenko, J.; Roldan Cuenya, B. Electrocatalyst Characterization by X-ray Absorption Spectroscopy. *Chem. Rev.* **2021**, *121*, 882–961. [[CrossRef](#)] [[PubMed](#)]
6. Anic, K.; Wolfbeisser, A.; Li, H.; Rameshan, C.; Föttinger, K.; Bernardi, J.; Rupprechter, G. Surface Spectroscopy on UHV-Grown and Technological Ni-ZrO<sub>2</sub> Reforming Catalysts: From UHV to Operando Conditions. *Top. Catal.* **2016**, *59*, 1614–1627. [[CrossRef](#)]
7. Mekhemer, G.A.H.; Mohamed, H.A.A.; Bumajdad, A.; Zaki, M.I. Lattice-Charge Imbalance and Redox Catalysis over Perovskite-Type Ferrite- and Manganite-Based Mixed Oxides as Studied by XRD, FTIR, UV-Vis DRS, and XPS. *Sci. Rep.* **2023**, *13*, 7453. [[CrossRef](#)]
8. Eijsbouts, S.; Van Den Oetelaar, L.C.A.; Rayner, M.; Govaers, H.; Boonen, T. Combined HR TEM and STEM-EDX Evaluation—The Key to Better Understanding of the Co-Mo Sulfide Active Phase in Real-Life Co-Mo-P/Al<sub>2</sub>O<sub>3</sub> Catalysts. *J. Catal.* **2021**, *403*, 56–73. [[CrossRef](#)]
9. Albertin, S.; Gustafson, J.; Zhou, J.; Pfaff, S.; Shipilin, M.; Blomberg, S.; Merte, L.R.; Gutowski, O.; Dippel, A.-C.; Zetterberg, J.; et al. Surface Optical Reflectance Combined with X-ray Techniques during Gas-Surface Interactions. *J. Phys. Appl. Phys.* **2020**, *53*, 224001. [[CrossRef](#)]
10. Hejral, U.; Shipilin, M.; Gustafson, J.; Stierle, A.; Lundgren, E. High Energy Surface X-ray Diffraction Applied to Model Catalyst Surfaces at Work. *J. Phys. Condens. Matter* **2021**, *33*, 073001. [[CrossRef](#)]
11. Merte, L.R.; Olsson, P.A.T.; Shipilin, M.; Gustafson, J.; Bertram, F.; Zhang, C.; Grönbeck, H.; Lundgren, E. Structure of Two-Dimensional Fe<sub>3</sub>O<sub>4</sub>. *J. Chem. Phys.* **2020**, *152*, 114705. [[CrossRef](#)] [[PubMed](#)]
12. Zimmerli, N.K.; Müller, C.R.; Abdala, P.M. Deciphering the Structure of Heterogeneous Catalysts across Scales Using Pair Distribution Function Analysis. *Trends Chem.* **2022**, *4*, 807–821. [[CrossRef](#)]
13. Terrill, N.J.; Dent, A.J.; Dobson, B.; Beale, A.M.; Allen, L.; Bras, W. Past, Present and Future—Sample Environments for Materials Research Studies in Scattering and Spectroscopy; a UK Perspective. *J. Phys. Condens. Matter* **2021**, *33*, 483002. [[CrossRef](#)]
14. Cheng, W.; Chen, Z.; Wu, X.; Wu, Z.; Wang, X.; Zhao, M.; Liu, H.; Jia, H.; Wang, C.; Wang, X.; et al. Anomalous Small-Angle X-ray Scattering and Its Application in the Dynamic Reconstruction of Electrochemical CO<sub>2</sub> Reduction Catalysts. *Symmetry* **2023**, *15*, 1034. [[CrossRef](#)]
15. Luo, Y.; Wu, Y. Defect Engineering of Nanomaterials for Catalysis. *Nanomaterials* **2023**, *13*, 1116. [[CrossRef](#)]
16. Pinto, F.M.; Suzuki, V.Y.; Silva, R.C.; La Porta, F.A. Oxygen Defects and Surface Chemistry of Reducible Oxides. *Front. Mater.* **2019**, *6*, 260. [[CrossRef](#)]

17. Masliuk, L.; Heggen, M.; Noack, J.; Girgsdies, F.; Trunschke, A.; Hermann, K.E.; Willinger, M.G.; Schlögl, R.; Lunkenbein, T. Structural Complexity in Heterogeneous Catalysis: Cataloging Local Nanostructures. *J. Phys. Chem. C* **2017**, *121*, 24093–24103. [[CrossRef](#)]
18. Zieliński, M.; Kaszkur, Z.; Juszczak, W.; Sobczak, J. In Situ Diffraction Monitoring of Nanocrystals Structure Evolving during Catalytic Reaction at Their Surface. *Sci. Rep.* **2023**, *13*, 1469. [[CrossRef](#)]
19. Nezhad, P.D.K.; Bekheet, M.F.; Bonmassar, N.; Schlicker, L.; Gili, A.; Kamutzki, F.; Gurlo, A.; Doran, A.; Gao, Y.; Heggen, M.; et al. Mechanistic In Situ Insights into the Formation, Structural and Catalytic Aspects of the  $\text{La}_2\text{NiO}_4$  Intermediate Phase in the Dry Reforming of Methane over Ni-Based Perovskite Catalysts. *Appl. Catal. Gen.* **2021**, *612*, 117984. [[CrossRef](#)]
20. Mutschler, R.; Moioli, E.; Zhao, K.; Lombardo, L.; Oveisi, E.; Porta, A.; Falbo, L.; Visconti, C.G.; Lietti, L.; Züttel, A. Imaging Catalysis: Operando Investigation of the  $\text{CO}_2$  Hydrogenation Reaction Dynamics by Means of Infrared Thermography. *ACS Catal.* **2020**, *10*, 1721–1730. [[CrossRef](#)]
21. Xu, X.; Wang, Q.; Xie, L.; Liu, Y.; Li, D.; Feng, J.; Duan, X. Thermal Effect Optimization Endows a Selective and Stable  $\text{PdCu}$  Single Atom Alloy Catalyst for Acetylene Hydrogenation. *AIChE J.* **2023**, *69*, e18042. [[CrossRef](#)]
22. Rochet, A.; Suzana, A.F.; Passos, A.R.; Kalile, T.; Berenguer, F.; Santilli, C.V.; Pulcinelli, S.H.; Meneau, F. In Situ Reactor to Image Catalysts at Work in Three-Dimensions by Bragg Coherent X-ray Diffraction. *Catal. Today* **2019**, *336*, 169–173. [[CrossRef](#)]
23. Becher, J.; Weber, S.; Ferreira Sanchez, D.; Doronkin, D.E.; Garrevoet, J.; Falkenberg, G.; Motta Meira, D.; Pasquarelli, S.; Grunwaldt, J.-D.; Sheppard, T.L. Sample Environment for Operando Hard X-ray Tomography—An Enabling Technology for Multimodal Characterization in Heterogeneous Catalysis. *Catalysts* **2021**, *11*, 459. [[CrossRef](#)]
24. Wollak, B.; Espinoza, D.; Dippel, A.-C.; Sturm, M.; Vrljic, F.; Gutowski, O.; Nielsen, I.G.; Sheppard, T.L.; Korup, O.; Horn, R. Catalytic Reactor for Spatially Resolved Structure–Activity Profiling Using High-Energy X-ray Diffraction. *J. Synchrotron Radiat.* **2023**, *30*, 571–581. [[CrossRef](#)] [[PubMed](#)]
25. Vermeulen, A.C. The Sensitivity of Focusing, Parallel Beam and Mixed Optics to Alignment Errors in XRD Residual Stress Measurements. *Mater. Sci. Forum* **2005**, *490–491*, 131–136. [[CrossRef](#)]
26. Zhao, P.; Lu, L.; Liu, X.; De La Torre, A.; Cheng, X. Error Analysis and Correction for Quantitative Phase Analysis Based on Rietveld-Internal Standard Method: Whether the Minor Phases Can Be Ignored? *Crystals* **2018**, *8*, 110. [[CrossRef](#)]
27. Moss, A.B.; Garg, S.; Mirolo, M.; Giron Rodriguez, C.A.; Ilvonen, R.; Chorkendorff, I.; Drnec, J.; Seger, B. In Operando Investigations of Oscillatory Water and Carbonate Effects in MEA-Based  $\text{CO}_2$  Electrolysis Devices. *Joule* **2023**, *7*, 350–365. [[CrossRef](#)]
28. Cats, K.H.; Weckhuysen, B.M. Combined Operando X-ray Diffraction/Raman Spectroscopy of Catalytic Solids in the Laboratory: The  $\text{Co}/\text{TiO}_2$  Fischer-Tropsch Synthesis Catalyst Showcase. *ChemCatChem* **2016**, *8*, 1531–1542. [[CrossRef](#)]
29. Sá, J.; Szlachetko, J. Heterogeneous Catalysis Experiments at XFELs. Are We Close to Producing a Catalysis Movie? *Catal. Lett.* **2014**, *144*, 197–203. [[CrossRef](#)]
30. Galler, A.; Gawelda, W.; Biednov, M.; Bomer, C.; Britz, A.; Brockhauser, S.; Choi, T.-K.; Diez, M.; Frankenberger, P.; French, M.; et al. Scientific Instrument Femtosecond X-ray Experiments (FXE): Instrumentation and Baseline Experimental Capabilities. *J. Synchrotron Radiat.* **2019**, *26*, 1432–1447. [[CrossRef](#)]
31. Wiedorn, M.O.; Awel, S.; Morgan, A.J.; Ayyer, K.; Fleckenstein, H.; Roth, N.; Adriano, L.; Bean, R.; Beyerlein, K.R.; et al. Rapid Sample Delivery for Megahertz Serial Crystallography at X-ray FELs. *IUCrJ* **2018**, *5*, 574–584. [[CrossRef](#)] [[PubMed](#)]
32. Raimondi, P.; Benabderrahmane, C.; Berkvens, P.; Biasci, J.C.; Borowiec, P.; Bouteille, J.-F.; Brochard, T.; Brookes, N.B.; Carmignani, N.; Carver, L.R.; et al. The Extremely Brilliant Source Storage Ring of the European Synchrotron Radiation Facility. *Commun. Phys.* **2023**, *6*, 82. [[CrossRef](#)] [[PubMed](#)]
33. Lo, B.T.W.; Ye, L.; Tsang, S.C.E. The Contribution of Synchrotron X-ray Powder Diffraction to Modern Zeolite Applications: A Mini-Review and Prospects. *Chem* **2018**, *4*, 1778–1808. [[CrossRef](#)]
34. Newton, M. Time Resolved Operando X-ray Techniques in Catalysis, a Case Study: CO Oxidation by  $\text{O}_2$  over Pt Surfaces and Alumina Supported Pt Catalysts. *Catalysts* **2017**, *7*, 58. [[CrossRef](#)]
35. Behling, R. *Modern Diagnostic X-ray Sources: Technology, Manufacturing, Reliability*, 2nd ed.; CRC Press: Boca Raton, FL, USA, 2021; ISBN 978-1-00-309540-8.
36. Yamada, H. The Smallest Electron Storage Ring for High-Intensity Far-Infrared and Hard X-ray Productions. *J. Synchrotron Radiat.* **1998**, *5*, 1326–1331. [[CrossRef](#)] [[PubMed](#)]
37. Rocha, J.G.; Lanceros-Mendez, S. Review on X-ray Detectors Based on Scintillators and CMOS Technology. *Recent Pat. Electr. Eng.* **2011**, *4*, 16–41. [[CrossRef](#)]
38. Kasap, S.; Frey, J.B.; Belev, G.; Tousignant, O.; Mani, H.; Greenspan, J.; Laperriere, L.; Bubon, O.; Reznik, A.; DeCrescenzo, G.; et al. Amorphous and Polycrystalline Photoconductors for Direct Conversion Flat Panel X-ray Image Sensors. *Sensors* **2011**, *11*, 5112–5157. [[CrossRef](#)]
39. Rosenfeld, A.; Silari, M.; Campbell, M. The Editorial. *Radiat. Meas.* **2020**, *139*, 106483. [[CrossRef](#)]
40. Aulchenko, V.M.; Evdokov, O.V.; Kutovenko, V.D.; Pirogov, B.Y.; Sharafutdinov, M.R.; Titov, V.M.; Tolochko, B.P.; Vasiljev, A.V.; Zhogin, I.A.; Zhulanov, V.V. One-Coordinate X-ray Detector OD-3M. *Nucl. Instrum. Methods Phys. Res. Sect. A* **2009**, *603*, 76–79. [[CrossRef](#)]
41. Ermrich, M.; Hahn, F.; Wölfel, E.R. Use of Imaging Plates in X-ray Analysis. *Textures Microstruct.* **1997**, *29*, 89–101. [[CrossRef](#)]

42. Rocha, J.G.; Goncalves, L.M.; Lanceros-Mendez, S. Flexible X-ray Detector Based on the Seebeck Effect. In Proceedings of the TRANSDUCERS 2009–2009 International Solid-State Sensors, Actuators and Microsystems Conference, Denver, CO, USA, 21–25 June 2009; IEEE: Denver, CO, USA, 2009; pp. 1967–1970.
43. Allé, P.; Wenger, E.; Dahaoui, S.; Schaniel, D.; Lecomte, C. Comparison of CCD, CMOS and Hybrid Pixel X-ray Detectors: Detection Principle and Data Quality. *Phys. Scr.* **2016**, *91*, 063001. [[CrossRef](#)]
44. Hodeau, J.-L.; Bordet, P.; Anne, M.; Prat, A.; Fitch, A.N.; Dooryhee, E.; Vaughan, G.; Freund, A.K. Nine-Crystal Multianalyzer Stage for High-Resolution Powder Diffraction between 6 keV and 40 keV, Proceedings of the SPIE’s International Symposium on Optical Science, Engineering, and Instrumentation, 19–24 July 1998, San Diego, CA, USA; Macrander, A.T., Freund, A.K., Ishikawa, T., Mills, D.M., Eds.; SPIE: San Diego, CA, USA, 1998; p. 353.
45. Thompson, S.P.; Parker, J.E.; Potter, J.; Hill, T.P.; Birt, A.; Cobb, T.M.; Yuan, F.; Tang, C.C. Beamline I11 at Diamond: A New Instrument for High Resolution Powder Diffraction. *Rev. Sci. Instrum.* **2009**, *80*, 075107. [[CrossRef](#)] [[PubMed](#)]
46. Drakopoulos, M.; Connolley, T.; Reinhard, C.; Atwood, R.; Magdysyuk, O.; Vo, N.; Hart, M.; Connor, L.; Humphreys, B.; Howell, G.; et al. I12: The Joint Engineering, Environment and Processing (JEEP) Beamline at Diamond Light Source. *J. Synchrotron Radiat.* **2015**, *22*, 828–838. [[CrossRef](#)]
47. Förster, A.; Brandstetter, S.; Schulze-Briese, C. Transforming X-ray Detection with Hybrid Photon Counting Detectors. *Philos. Trans. R. Soc. Math. Phys. Eng. Sci.* **2019**, *377*, 20180241. [[CrossRef](#)] [[PubMed](#)]
48. Brönnimann, C.; Trüb, P. Hybrid Pixel Photon Counting X-ray Detectors for Synchrotron Radiation. In *Synchrotron Light Sources and Free-Electron Lasers*; Jaeschke, E., Khan, S., Schneider, J.R., Hastings, J.B., Eds.; Springer International Publishing: Cham, Switzerland, 2015; pp. 1–29. ISBN 978-3-319-04507-8.
49. Volkov, S.; Vonk, V.; Khorshidi, N.; Franz, D.; Kubicek, M.; Kilic, V.; Felici, R.; Huber, T.M.; Navickas, E.; Rupp, G.M.; et al. Operando X-ray Investigation of Electrode/Electrolyte Interfaces in Model Solid Oxide Fuel Cells. *Chem. Mater.* **2016**, *28*, 3727–3733. [[CrossRef](#)] [[PubMed](#)]
50. Alabdulkarim, M.E.; Maxwell, W.D.; Thapliyal, V.; Maxwell, J.L. A Comprehensive Review of High-Pressure Laser-Induced Materials Processing, Part I: Laser-Heated Diamond Anvil Cells. *J. Manuf. Mater. Process.* **2022**, *6*, 111. [[CrossRef](#)]
51. Saraev, A.A.; Vinokurov, Z.S.; Kaichev, V.V.; Shmakov, A.N.; Bukhtiyarov, V.I. The Origin of Self-Sustained Reaction-Rate Oscillations in the Oxidation of Methane over Nickel: An Operando XRD and Mass Spectrometry Study. *Catal. Sci. Technol.* **2017**, *7*, 1646–1649. [[CrossRef](#)]
52. Wu, H.; Stacey, D. Small- and Wide-Angle X-ray Scattering (SAXS/WAXS) with Temperature-Controlled Stages Makes Phase Identification Faster than Ever. *Microsc. Today* **2021**, *29*, 30–36. [[CrossRef](#)]
53. Saleta, M.E.; Eleotério, M.; Mesquita, A.; Mastelaro, V.R.; Granado, E. Atomic Pair Distribution Function at the Brazilian Synchrotron Light Laboratory: Application to the  $Pb_{1-x}La_xZr_{0.40}Ti_{0.60}O_3$  Ferroelectric System. *J. Synchrotron Radiat.* **2017**, *24*, 1098–1104. [[CrossRef](#)]
54. Chiarello, G.L.; Nachtegaal, M.; Marchionni, V.; Quaroni, L.; Ferri, D. Adding Diffuse Reflectance Infrared Fourier Transform Spectroscopy Capability to Extended X-ray-Absorption Fine Structure in a New Cell to Study Solid Catalysts in Combination with a Modulation Approach. *Rev. Sci. Instrum.* **2014**, *85*, 074102. [[CrossRef](#)]
55. Rothensteiner, M.; Jenni, J.; Emerich, H.; Bonk, A.; Vogt, U.F.; Van Bokhoven, J.A. In Situ Flow Cell for Combined X-ray Absorption Spectroscopy, X-ray Diffraction, and Mass Spectrometry at High Photon Energies under Solar Thermochemical Looping Conditions. *Rev. Sci. Instrum.* **2017**, *88*, 083116. [[CrossRef](#)]
56. Baimpas, N.; Drakopoulos, M.; Connolley, T.; Song, X.; Pandazaras, C.; Korsunsky, A.M. A Feasibility Study of Dynamic Stress Analysis inside a Running Internal Combustion Engine Using Synchrotron X-ray Beams. *J. Synchrotron Radiat.* **2013**, *20*, 316–323. [[CrossRef](#)]
57. Čajka, T.; Hajšlová, J.; Kazda, R.; Poustka, J. Challenges of Gas Chromatography-High-Resolution Time-of-Flight Mass Spectrometry for Simultaneous Analysis of Polybrominated Diphenyl Ethers and Other Halogenated Persistent Organic Pollutants in Environmental Samples. *J. Sep. Sci.* **2005**, *28*, 601–611. [[CrossRef](#)] [[PubMed](#)]
58. Hejazi, L.; Ebrahimi, D.; Hibbert, D.B.; Guilhaus, M. Compatibility of Electron Ionization and Soft Ionization Methods in Gas Chromatography/Orthogonal Time-of-Flight Mass Spectrometry: EI and Soft Ionization Methods in GC/Oa-TOFMS. *Rapid Commun. Mass Spectrom.* **2009**, *23*, 2181–2189. [[CrossRef](#)] [[PubMed](#)]
59. Pan, Y.; Zhang, L.; Zhang, T.; Guo, H.; Hong, X.; Qi, F. Photoionization Studies on Various Quinones by an Infrared Laser Desorption/Tunable VUV Photoionization TOF Mass Spectrometry. *J. Mass Spectrom.* **2008**, *43*, 1701–1710. [[CrossRef](#)]
60. Mukarakate, C.; Scheer, A.M.; Robichaud, D.J.; Jarvis, M.W.; David, D.E.; Ellison, G.B.; Nimlos, M.R.; Davis, M.F. Laser Ablation with Resonance-Enhanced Multiphoton Ionization Time-of-Flight Mass Spectrometry for Determining Aromatic Lignin Volatilization Products from Biomass. *Rev. Sci. Instrum.* **2011**, *82*, 033104. [[CrossRef](#)]
61. Bicchi, C.; Brunelli, C.; Galli, M.; Sironi, A. Conventional Inner Diameter Short Capillary Columns: An Approach to Speeding up Gas Chromatographic Analysis of Medium Complexity Samples. *J. Chromatogr. A* **2001**, *931*, 129–140. [[CrossRef](#)] [[PubMed](#)]
62. van Deursen, M.M.; Beens, J.; Janssen, H.-G.; Leclercq, P.A.; Cramers, C.A. Evaluation of Time-of-Flight Mass Spectrometric Detection for Fast Gas Chromatography. *J. Chromatogr. A* **2000**, *878*, 205–213. [[CrossRef](#)]
63. Van Deursen, M.; Janssen, H.-G.; Beens, J.; Lipman, P.; Reinierkens, R.; Rutten, G.; Cramers, C. Fast Gas Chromatography Using Vacuum Outlet Conditions. *J. Microcolumn Sep.* **2000**, *12*, 613–622. [[CrossRef](#)]

64. Tranchida, P.Q.; Zoccali, M.; Mondello, L. High-Speed GC-MS. In *Hyphenations of Capillary Chromatography with Mass Spectrometry*; Elsevier: Amsterdam, The Netherlands, 2020; pp. 109–132. ISBN 978-0-12-809638-3.
65. Gates-Rector, S.; Blanton, T. The Powder Diffraction File: A Quality Materials Characterization Database. *Powder Diffr.* **2019**, *34*, 352–360. [[CrossRef](#)]
66. Cranswick, L.M.D. Chapter 17. Computer Software for Powder Diffraction. In *Powder Diffraction*; Dinnebier, R.E., Billinge, S.J.L., Eds.; Royal Society of Chemistry: Cambridge, UK, 2008; pp. 494–570. ISBN 978-0-85404-231-9.
67. Johny, J.; Prymak, O.; Kamp, M.; Calvo, F.; Kim, S.-H.; Tymoczko, A.; El-Zoka, A.; Rehbock, C.; Schürmann, U.; Gault, B.; et al. Multidimensional Thermally-Induced Transformation of Nest-Structured Complex Au-Fe Nanoalloys towards Equilibrium. *Nano Res.* **2022**, *15*, 581–592. [[CrossRef](#)]
68. Larsson, A.; Abbondanza, G.; Rämisch, L.; Linpé, W.; Novikov, D.V.; Lundgren, E.; Harlow, G.S. In Situ Scanning X-ray Diffraction Reveals Strain Variations in Electrochemically Grown Nanowires. *J. Phys. Appl. Phys.* **2021**, *54*, 235301. [[CrossRef](#)]
69. Slowik, G.; Gawryszuk-Rżysko, A.; Greluk, M.; Machocki, A. Estimation of Average Crystallites Size of Active Phase in Ceria-Supported Cobalt-Based Catalysts by Hydrogen Chemisorption vs TEM and XRD Methods. *Catal. Lett.* **2016**, *146*, 2173–2184. [[CrossRef](#)]
70. Langford, J.I.; Wilson, A.J.C. Scherrer after Sixty Years: A Survey and Some New Results in the Determination of Crystallite Size. *J. Appl. Crystallogr.* **1978**, *11*, 102–113. [[CrossRef](#)]
71. Williamson, G.K.; Hall, W.H. X-ray Line Broadening from Filed Aluminium and Wolfram. *Acta Metall.* **1953**, *1*, 22–31. [[CrossRef](#)]
72. Rietveld, H.M. A Profile Refinement Method for Nuclear and Magnetic Structures. *J. Appl. Crystallogr.* **1969**, *2*, 65–71. [[CrossRef](#)]
73. Davies, R.J. A New Batch-Processing Data-Reduction Application for X-ray Diffraction Data. *J. Appl. Crystallogr.* **2006**, *39*, 267–272. [[CrossRef](#)]
74. Stinton, G.W.; Evans, J.S.O. Parametric Rietveld Refinement. *J. Appl. Crystallogr.* **2007**, *40*, 87–95. [[CrossRef](#)]
75. Schuetzke, J.; Benedix, A.; Mikut, R.; Reischl, M. Enhancing Deep-Learning Training for Phase Identification in Powder X-ray Diffractograms. *IUCrJ* **2021**, *8*, 408–420. [[CrossRef](#)]
76. Wang, H.; Xie, Y.; Li, D.; Deng, H.; Zhao, Y.; Xin, M.; Lin, J. Rapid Identification of X-ray Diffraction Patterns Based on Very Limited Data by Interpretable Convolutional Neural Networks. *J. Chem. Inf. Model.* **2020**, *60*, 2004–2011. [[CrossRef](#)]
77. Oviedo, F.; Ren, Z.; Sun, S.; Settens, C.; Liu, Z.; Hartono, N.T.P.; Ramasamy, S.; DeCost, B.L.; Tian, S.I.P.; Romano, G.; et al. Fast and Interpretable Classification of Small X-ray Diffraction Datasets Using Data Augmentation and Deep Neural Networks. *npj Comput. Mater.* **2019**, *5*, 60. [[CrossRef](#)]
78. Lee, J.-W.; Park, W.B.; Kim, M.; Pal Singh, S.; Pyo, M.; Sohn, K.-S. A Data-Driven XRD Analysis Protocol for Phase Identification and Phase-Fraction Prediction of Multiphase Inorganic Compounds. *Inorg. Chem. Front.* **2021**, *8*, 2492–2504. [[CrossRef](#)]
79. Baylet, A.; Marécot, P.; Duprez, D.; Castellazzi, P.; Groppi, G.; Forzatti, P. In Situ Raman and In Situ XRD Analysis of PdO Reduction and Pd<sup>0</sup> Oxidation Supported on γ-Al<sub>2</sub>O<sub>3</sub> Catalyst under Different Atmospheres. *Phys. Chem. Chem. Phys.* **2011**, *13*, 4607. [[CrossRef](#)]
80. Kulbakov, A.A.; Kuriganova, A.B.; Allix, M.; Rakhmatullin, A.; Smirnova, N.V.; Maslova, O.A.; Leontyev, I.N. Non-Isothermal Decomposition of Platinum Acetylacetone as a Cost-Efficient and Size-Controlled Synthesis of Pt/C Nanoparticles. *Catal. Commun.* **2018**, *117*, 14–18. [[CrossRef](#)]
81. Zadesenets, A.V.; Garkul, I.A.; Filatov, E.Y.; Plyusnin, P.E.; Filippov, T.N.; Asanova, T.I.; Korolkov, I.V.; Baidina, I.A.; Asanov, I.P.; Korenev, S.V. Oxalato Complexes of Pd(II) with Co(II) and Ni(II) as Single-Source Precursors for Bimetallic Nanoalloys. *J. Therm. Anal. Calorim.* **2019**, *138*, 111–121. [[CrossRef](#)]
82. Kardash, T.Y.; Plyasova, L.M.; Bondareva, V.M.; Andrushkevich, T.V.; Ishchenko, A.V.; Chesalov, Y.A.; Dovlitova, L.S. Effect of Thermal Treatment Conditions on the Phase Composition and Structural Characteristics of V-Mo-Nb-O Catalysts. *Kinet. Catal.* **2009**, *50*, 48–56. [[CrossRef](#)]
83. Girgsdies, F.; Schlögl, R.; Trunschke, A. In-Situ X-ray Diffraction Study of Phase Crystallization from an Amorphous MoVTeNb Oxide Catalyst Precursor. *Catal. Commun.* **2012**, *18*, 60–62. [[CrossRef](#)]
84. Kardash, T.Y.; Lazareva, E.V.; Svintsitskiy, D.A.; Kovalev, E.P.; Bondareva, V.M. Effect of Selenium Additives on the Physicochemical and Catalytic Properties of VMoTeNbO Catalysts in the Oxidative Dehydrogenation of Ethane. *Kinet. Catal.* **2019**, *60*, 355–365. [[CrossRef](#)]
85. Norby, P.; Hanson, J.C. Hydrothermal Synthesis of the Microporous Aluminophosphate CoAPO-5; In Situ Time-Resolved Synchrotron X-ray Powder Diffraction Studies. *Catal. Today* **1998**, *39*, 301–309. [[CrossRef](#)]
86. Norby, P. In-Situ XRD as a Tool to Understanding Zeolite Crystallization. *Curr. Opin. Colloid Interface Sci.* **2006**, *11*, 118–125. [[CrossRef](#)]
87. Tsibulya, S.V. Structural Aspect of a Thermal Activation Effect in the MnO<sub>x</sub>/γ-Al<sub>2</sub>O<sub>3</sub> System. *Kinet. Catal.* **2003**, *44*, 287–296. [[CrossRef](#)]
88. Bulavchenko, O.A.; Afonasenko, T.N.; Tsyrul'nikov, P.G.; Tsibulya, S.V. Effect of Heat Treatment Conditions on the Structure and Catalytic Properties of MnO/Al<sub>2</sub>O<sub>3</sub> in the Reaction of CO Oxidation. *Appl. Catal. Gen.* **2013**, *459*, 73–80. [[CrossRef](#)]
89. Cherepanova, S.V.; Bulavchenko, O.A.; Gerasimov, E.Y.; Tsibulya, S.V. Low- and High-Temperature Oxidation of Mn<sub>1.5</sub>Al<sub>1.5</sub>O<sub>4</sub> in Relation to Decomposition Mechanism and Microstructure. *CrystEngComm* **2016**, *18*, 3411–3421. [[CrossRef](#)]
90. Bulavchenko, O.A.; Tsibulya, S.V.; Cherepanova, S.V.; Afonasenko, T.N.; Tsyrulnikov, P.G. High-Temperature X-ray Study of the Formation and Delamination of Manganese-Alumina Spinel Mn<sub>1.5</sub>Al<sub>1.5</sub>O<sub>4</sub>. *J. Struct. Chem.* **2009**, *50*, 474–478. [[CrossRef](#)]

91. Bulavchenko, O.A.; Afonasenko, T.N.; Vinokurov, Z.S.; Pochtar, A.A.; Rogov, V.A.; Tsybulya, S.V. The Thermal Activation of  $MnO_x-Al_2O_3$  Catalysts: Effect of Gallium Doping. *Mater. Chem. Phys.* **2022**, *291*, 126715. [[CrossRef](#)]
92. Sietsma, J.R.A.; Friedrich, H.; Broersma, A.; Versluijs-Helder, M.; Jos Van Dillen, A.; De Jongh, P.E.; De Jong, K.P. How Nitric Oxide Affects the Decomposition of Supported Nickel Nitrate to Arrive at Highly Dispersed Catalysts. *J. Catal.* **2008**, *260*, 227–235. [[CrossRef](#)]
93. Munnik, P.; Wolters, M.; Gabrielsson, A.; Pollington, S.D.; Headdock, G.; Bitter, J.H.; De Jongh, P.E.; De Jong, K.P. Copper Nitrate Redispersion to Arrive at Highly Active Silica-Supported Copper Catalysts. *J. Phys. Chem. C* **2011**, *115*, 14698–14706. [[CrossRef](#)]
94. Mao, X.; Xia, X.; Li, J.; Chen, C.; Gu, X.; Li, S.; Lan, Y.-P. Self-Assembly of Structured  $CeCO_3OH$  and Its Decomposition in  $H_2$  for a Novel Tactic to Obtain  $CeO_{2-x}$  with Excellent Photocatalytic Property. *J. Alloys Compd.* **2021**, *870*, 159424. [[CrossRef](#)]
95. Bulavchenko, O.A.; Vinokurov, Z.S.; Nikolaeva, O.A.; Afonasenko, T.N.; Tsybulya, S.V. STUDY OF THERMAL CO-DECOMPOSITION OF MANGANESE AND CERIUM OXALATES IN AIR AND IN INERT MEDIA. *J. Struct. Chem.* **2021**, *62*, 467–480. [[CrossRef](#)]
96. Mamede, A. Characterization of  $WO_x/CeO_2$  Catalysts and Their Reactivity in the Isomerization of Hexane. *J. Catal.* **2004**, *223*, 1–12. [[CrossRef](#)]
97. Holmgreen, E.M.; Yung, M.M.; Ozkan, U.S. Pd-Based Sulfated Zirconia Prepared by a Single Step Sol-Gel Procedure for Lean  $NO_x$  Reduction. *J. Mol. Catal. Chem.* **2007**, *270*, 101–111. [[CrossRef](#)]
98. Lagunova, V.I.; Filatov, E.Y.; Plyusnin, P.E.; Korenev, S.V. In Situ and Ex Situ Studies of Tetrammineplatinum(II) Chromate Thermolysis. *Russ. J. Inorg. Chem.* **2020**, *65*, 1566–1570. [[CrossRef](#)]
99. Shen, X.-F.; Ding, Y.-S.; Hanson, J.C.; Aindow, M.; Suib, S.L. In Situ Synthesis of Mixed-Valent Manganese Oxide Nanocrystals: An In Situ Synchrotron X-ray Diffraction Study. *J. Am. Chem. Soc.* **2006**, *128*, 4570–4571. [[CrossRef](#)] [[PubMed](#)]
100. Heidari, S.; Balaghi, S.E.; Sologubenko, A.S.; Patzke, G.R. Economic Manganese-Oxide-Based Anodes for Efficient Water Oxidation: Rapid Synthesis and In Situ Transmission Electron Microscopy Monitoring. *ACS Catal.* **2021**, *11*, 2511–2523. [[CrossRef](#)]
101. Ruiz Puigdollers, A.; Schlexer, P.; Tosoni, S.; Pacchioni, G. Increasing Oxide Reducibility: The Role of Metal/Oxide Interfaces in the Formation of Oxygen Vacancies. *ACS Catal.* **2017**, *7*, 6493–6513. [[CrossRef](#)]
102. Lukashuk, L.; Yigit, N.; Rameshan, R.; Kolar, E.; Teschner, D.; Hävecker, M.; Knop-Gericke, A.; Schlögl, R.; Föttinger, K.; Rupprechter, G. Operando Insights into CO Oxidation on Cobalt Oxide Catalysts by NAP-XPS, FTIR, and XRD. *ACS Catal.* **2018**, *8*, 8630–8641. [[CrossRef](#)]
103. Dionigi, F.; Zeng, Z.; Sinev, I.; Merzdorf, T.; Deshpande, S.; Lopez, M.B.; Kunze, S.; Zegkinoglou, I.; Sarodnik, H.; Fan, D.; et al. In-Situ Structure and Catalytic Mechanism of NiFe and CoFe Layered Double Hydroxides during Oxygen Evolution. *Nat. Commun.* **2020**, *11*, 2522. [[CrossRef](#)] [[PubMed](#)]
104. Rochet, A.; Moizan, V.; Pichon, C.; Diehl, F.; Berliet, A.; Briois, V. In Situ and Operando Structural Characterisation of a Fischer-Tropsch Supported Cobalt Catalyst. *Catal. Today* **2011**, *171*, 186–191. [[CrossRef](#)]
105. Jalama, K.; Kabuba, J.; Xiong, H.; Jewell, L.L. Co/TiO<sub>2</sub> Fischer-Tropsch Catalyst Activation by Synthesis Gas. *Catal. Commun.* **2012**, *17*, 154–159. [[CrossRef](#)]
106. Khassin, A.A.; Simentsova, I.I.; Shmakov, A.N.; Shtertser, N.V.; Bulavchenko, O.A.; Cherepanova, S.V. Effect of Nitric Oxide on the Formation of Cobalt–Aluminum Oxide Structure from Layered Double Hydroxide and Its Further Transformation during Reductive Activation. *Appl. Catal. Gen.* **2016**, *514*, 114–125. [[CrossRef](#)]
107. Popa, T.; Xu, G.; Barton, T.F.; Argyle, M.D. High Temperature Water Gas Shift Catalysts with Alumina. *Appl. Catal. Gen.* **2010**, *379*, 15–23. [[CrossRef](#)]
108. Reddy, G.K.; Gunasekara, K.; Boolchand, P.; Smirniotis, P.G. Cr- and Ce-Doped Ferrite Catalysts for the High Temperature Water–Gas Shift Reaction: TPR and Mossbauer Spectroscopic Study. *J. Phys. Chem. C* **2011**, *115*, 920–930. [[CrossRef](#)]
109. Kaichev, V.V.; Chesalov, Y.A.; Saraev, A.A.; Tsapina, A.M. A Mechanistic Study of Dehydrogenation of Propane over Vanadia-Titania Catalysts. *J. Phys. Chem. C* **2019**, *123*, 19668–19680. [[CrossRef](#)]
110. Toko, K.; Ito, K.; Saito, H.; Hosono, Y.; Murakami, K.; Misaki, S.; Higo, T.; Ogo, S.; Tsuneki, H.; Maeda, S.; et al. Catalytic Dehydrogenation of Ethane over Doped Perovskite via the Mars–van Krevelen Mechanism. *J. Phys. Chem. C* **2020**, *124*, 10462–10469. [[CrossRef](#)]
111. Pussacq, T.; Mentré, O.; Tessier, F.; Löfberg, A.; Huvé, M.; Guerro Caballero, J.; Colis, S.; Kabbour, H. Nanometric Nickel Exsolution in the Hexagonal Perovskite  $Ba_8Ta_6NiO_{24}$ : Survey of the Structural, Magnetic and Catalytic Features. *J. Alloys Compd.* **2018**, *766*, 987–993. [[CrossRef](#)]
112. Kabbour, H.; Gauthier, G.H.; Tessier, F.; Huvé, M.; Pussacq, T.; Roussel, P.; Hayward, M.A.; Moreno B, Z.L.; Marinova, M.; Colmont, M.; et al. Topochemical Reduction of  $YMnO_3$  into a Composite Structure. *Inorg. Chem.* **2017**, *56*, 8547–8553. [[CrossRef](#)]
113. Gawande, M.B.; Goswami, A.; Felpin, F.-X.; Asefa, T.; Huang, X.; Silva, R.; Zou, X.; Zboril, R.; Varma, R.S. Cu and Cu-Based Nanoparticles: Synthesis and Applications in Catalysis. *Chem. Rev.* **2016**, *116*, 3722–3811. [[CrossRef](#)]
114. Sabat, K.C.; Paramguru, R.K.; Mishra, B.K. Reduction of Copper Oxide by Low-Temperature Hydrogen Plasma. *Plasma Chem. Plasma Process.* **2016**, *36*, 1111–1124. [[CrossRef](#)]
115. Rodriguez, J.A.; Kim, J.Y.; Hanson, J.C.; Pérez, M.; Frenkel, A.I. Reduction of CuO in  $H_2$ : In Situ Time-Resolved XRD Studies. *Catal. Lett.* **2003**, *85*, 247–254. [[CrossRef](#)]
116. Kim, J.Y.; Rodriguez, J.A.; Hanson, J.C.; Frenkel, A.I.; Lee, P.L. Reduction of CuO and  $Cu_2O$  with  $H_2$ : H Embedding and Kinetic Effects in the Formation of Suboxides. *J. Am. Chem. Soc.* **2003**, *125*, 10684–10692. [[CrossRef](#)]

117. Pike, J.; Chan, S.-W.; Zhang, F.; Wang, X.; Hanson, J. Formation of Stable Cu<sub>2</sub>O from Reduction of CuO Nanoparticles. *Appl. Catal. Gen.* **2006**, *303*, 273–277. [[CrossRef](#)]
118. Unutulmazsoy, Y.; Cancellieri, C.; Lin, L.; Jeurgens, L.P.H. Reduction of Thermally Grown Single-Phase CuO and Cu<sub>2</sub>O Thin Films by In-Situ Time-Resolved XRD. *Appl. Surf. Sci.* **2022**, *588*, 152896. [[CrossRef](#)]
119. Svintsitskiy, D.A.; Kardash, T.Y.; Stonkus, O.A.; Slavinskaya, E.M.; Stadnichenko, A.I.; Koscheev, S.V.; Chupakhin, A.P.; Boronin, A.I. In Situ XRD, XPS, TEM, and TPR Study of Highly Active in CO Oxidation CuO Nanopowders. *J. Phys. Chem. C* **2013**, *117*, 14588–14599. [[CrossRef](#)]
120. Den Breejen, J.P.; Radstake, P.B.; Bezemer, G.L.; Bitter, J.H.; Frøseth, V.; Holmen, A.; De Jong, K.P. On the Origin of the Cobalt Particle Size Effects in Fischer–Tropsch Catalysis. *J. Am. Chem. Soc.* **2009**, *131*, 7197–7203. [[CrossRef](#)]
121. Nematollahi, B.; Rezaei, M.; Lay, E.N. Preparation of Highly Active and Stable NiO–CeO<sub>2</sub> Nanocatalysts for CO Selective Methanation. *Int. J. Hydrogen Energy* **2015**, *40*, 8539–8547. [[CrossRef](#)]
122. Edwards, M.A.; Whittle, D.M.; Rhodes, C.; Ward, A.M.; Rohan, D.; Shannon, M.D.; Hutchings, G.J.; Kiely, C.J. Microstructural Studies of the Copper Promoted Iron Oxide/Chromia Water-Gas Shift Catalyst. *Phys. Chem. Chem. Phys.* **2002**, *4*, 3902–3908. [[CrossRef](#)]
123. He, M.; Luo, M.; Fang, P. Characterization of CuO Species and Thermal Solid-Solid Interaction in CuO/CeO<sub>2</sub>-Al<sub>2</sub>O<sub>3</sub> Catalyst by In-Situ XRD, Raman Spectroscopy and TPR. *J. Rare Earths* **2006**, *24*, 188–192. [[CrossRef](#)]
124. Du, H.; Ma, X.; Yan, P.; Jiang, M.; Zhao, Z.; Zhang, Z.C. Catalytic Furfural Hydrogenation to Furfuryl Alcohol over Cu/SiO<sub>2</sub> Catalysts: A Comparative Study of the Preparation Methods. *Fuel Process. Technol.* **2019**, *193*, 221–231. [[CrossRef](#)]
125. Luo, M.-F.; Fang, P.; He, M.; Xie, Y.-L. In Situ XRD, Raman, and TPR Studies of CuO/Al<sub>2</sub>O<sub>3</sub> Catalysts for CO Oxidation. *J. Mol. Catal. Chem.* **2005**, *239*, 243–248. [[CrossRef](#)]
126. Plyasova, L.M.; Kardash, T.Y.; Svintsitskiy, D.A.; Paukshtis, E.A.; Shtertser, N.V.; Minyukova, T.P. The Interaction of Copper-Containing Spinels CuFe<sub>2</sub>O<sub>4</sub> and CuFeCrO<sub>4</sub> with Hydrogen. *Mater. Res. Bull.* **2019**, *118*, 110481. [[CrossRef](#)]
127. Estrella, M.; Barrio, L.; Zhou, G.; Wang, X.; Wang, Q.; Wen, W.; Hanson, J.C.; Frenkel, A.I.; Rodriguez, J.A. In Situ Characterization of CuFe<sub>2</sub>O<sub>4</sub> and Cu/Fe<sub>3</sub>O<sub>4</sub> Water–Gas Shift Catalysts. *J. Phys. Chem. C* **2009**, *113*, 14411–14417. [[CrossRef](#)]
128. Wang, X.; Rodriguez, J.A.; Hanson, J.C.; Gamarra, D.; Martínez-Arias, A.; Fernández-García, M. Unusual Physical and Chemical Properties of Cu in Ce<sub>1-x</sub>Cu<sub>x</sub>O<sub>2</sub> Oxides. *J. Phys. Chem. B* **2005**, *109*, 19595–19603. [[CrossRef](#)] [[PubMed](#)]
129. Barbier, A.; Tuel, A.; Arcon, I.; Kodre, A.; Martin, G.A. Characterization and Catalytic Behavior of Co/SiO<sub>2</sub> Catalysts: Influence of Dispersion in the Fischer–Tropsch Reaction. *J. Catal.* **2001**, *200*, 106–116. [[CrossRef](#)]
130. Bezemer, G.L.; Bitter, J.H.; Kuipers, H.P.C.E.; Oosterbeek, H.; Holewijn, J.E.; Xu, X.; Kapteijn, F.; Van Dillen, A.J.; De Jong, K.P. Cobalt Particle Size Effects in the Fischer–Tropsch Reaction Studied with Carbon Nanofiber Supported Catalysts. *J. Am. Chem. Soc.* **2006**, *128*, 3956–3964. [[CrossRef](#)] [[PubMed](#)]
131. Bezemer, G.; Radstake, P.; Koot, V.; Vandullen, A.; Geus, J.; Dejong, K. Preparation of Fischer–Tropsch Cobalt Catalysts Supported on Carbon Nanofibers and Silica Using Homogeneous Deposition-Precipitation. *J. Catal.* **2006**, *237*, 291–302. [[CrossRef](#)]
132. Radstake, P.B.; Breejen, J.P.D.; Bezemer, G.L.; Bitter, J.H.; Jong, K.P.D.; Frøseth, V.; Holmen, A. On the Origin of the Cobalt Particle Size Effect in the Fischer-Tropsch Synthesis. In *Studies in Surface Science and Catalysis*; Elsevier: Amsterdam, The Netherlands, 2007; Volume 167, pp. 85–90. ISBN 978-0-444-53078-3.
133. Panda, A.; Kim, E.; Choi, Y.; Lee, J.; Venkateswarlu, S.; Yoon, M. Phase Controlled Synthesis of Pt Doped Co Nanoparticle Composites Using a Metal-Organic Framework for Fischer–Tropsch Catalysis. *Catalysts* **2019**, *9*, 156. [[CrossRef](#)]
134. Liu, L.; Qin, C.; Yu, M.; Wang, Q.; Wang, J.; Hou, B.; Jia, L.; Li, D. Morphology Evolution of Hcp Cobalt Nanoparticles Induced by Ru Promoter. *ChemCatChem* **2020**, *12*, 2083–2090. [[CrossRef](#)]
135. Gholami, Z.; Tišler, Z.; Rubáš, V. Recent Advances in Fischer-Tropsch Synthesis Using Cobalt-Based Catalysts: A Review on Supports, Promoters, and Reactors. *Catal. Rev.* **2021**, *63*, 512–595. [[CrossRef](#)]
136. Guo, S.; Ma, Z.; Wang, J.; Hou, B.; Jia, L.; Wang, B.; Li, D. Exploring the Reasons for Zr-Improved Performance of Alumina Supported Cobalt Fischer-Tropsch Synthesis. *J. Energy Inst.* **2021**, *96*, 31–37. [[CrossRef](#)]
137. Suo, Y.; Yao, Y.; Zhang, Y.; Xing, S.; Yuan, Z.-Y. Recent Advances in Cobalt-Based Fischer-Tropsch Synthesis Catalysts. *J. Ind. Eng. Chem.* **2022**, *115*, 92–119. [[CrossRef](#)]
138. Bulavchenko, O.A.; Cherepanova, S.V.; Malakhov, V.V.; Dovlitova, L.S.; Ishchenko, A.V.; Tsybulya, S.V. In Situ XRD Study of Nanocrystalline Cobalt Oxide Reduction. *Kinet. Catal.* **2009**, *50*, 192–198. [[CrossRef](#)]
139. Khodakov, A.Y.; Lynch, J.; Bazin, D.; Rebours, B.; Zanier, N.; Moisson, B.; Chaumette, P. Reducibility of Cobalt Species In Silica-Supported Fischer–Tropsch Catalysts. *J. Catal.* **1997**, *168*, 16–25. [[CrossRef](#)]
140. Zhang, Z.-S.; Fu, X.-P.; Wang, W.-W.; Jin, Z.; Song, Q.-S.; Jia, C.-J. Promoted Porous Co<sub>3</sub>O<sub>4</sub>-Al<sub>2</sub>O<sub>3</sub> Catalysts for Ammonia Decomposition. *Sci. China Chem.* **2018**, *61*, 1389–1398. [[CrossRef](#)]
141. Cherepanova, S.; Bulavchenko, O.; Simentsova, I.; Gerasimov, E.; Khassin, A. Influence of Al Ions on the Reduction of Co<sub>3-x</sub>Al<sub>x</sub>O<sub>4</sub>: In Situ XRD Investigation. In Proceedings of the European Powder Diffraction Conference, Darmstadt, Germany, 27–30 August 2010; Oldenbourg Wissenschaftsverlag: München, Germany, 2011; pp. 331–336, ISBN 978-3-486-98940-3.
142. Wang, J.; Wang, J.; Huang, X.; Chen, C.; Ma, Z.; Jia, L.; Hou, B.; Li, D. Co Al Spinel Oxide Modified Ordered Mesoporous Alumina Supported Cobalt-Based Catalysts for Fischer–Tropsch Synthesis. *Int. J. Hydrogen Energy* **2018**, *43*, 13122–13132. [[CrossRef](#)]
143. Van Deelen, T.W.; Yoshida, H.; Oord, R.; Zečević, J.; Weckhuysen, B.M.; De Jong, K.P. Cobalt Nanocrystals on Carbon Nanotubes in the Fischer-Tropsch Synthesis: Impact of Support Oxidation. *Appl. Catal. Gen.* **2020**, *593*, 117441. [[CrossRef](#)]

144. Bulavchenko, O.A.; Gerasimov, E.Y.; Afonasenko, T.N. Reduction of Double Manganese–Cobalt Oxides: In Situ XRD and TPR Study. *Dalton Trans.* **2018**, *47*, 17153–17159. [[CrossRef](#)]
145. Bulavchenko, O.A.; Afonasenko, T.N.; Ivanchikova, A.V.; Murzin, V.Y.; Kremneva, A.M.; Saraev, A.A.; Kaichev, V.V.; Tsibulya, S.V. In Situ Study of Reduction of  $Mn_xCo_{3-x}O_4$  Mixed Oxides: The Role of Manganese Content. *Inorg. Chem.* **2021**, *60*, 16518–16528. [[CrossRef](#)]
146. Wang, J.; Chernavskii, P.A.; Khodakov, A.Y.; Wang, Y. Structure and Catalytic Performance of Alumina-Supported Copper–Cobalt Catalysts for Carbon Monoxide Hydrogenation. *J. Catal.* **2012**, *286*, 51–61. [[CrossRef](#)]
147. Ciotonea, C.; Chiriac, A.; Dragoi, B.; Dhainaut, J.; Marinova, M.; Pronier, S.; Arii-Clacens, S.; Dacquin, J.-P.; Dumitriu, E.; Ungureanu, A.; et al. Playing on 3D Spatial Distribution of Cu-Co (Oxide) Nanoparticles in Inorganic Mesoporous Sieves: Impact on Catalytic Performance toward the Cinnamaldehyde Hydrogenation. *Appl. Catal. Gen.* **2021**, *623*, 118303. [[CrossRef](#)]
148. Kungurova, O.A.; Shtertser, N.V.; Koemets, E.G.; Cherepanova, S.V.; Khassin, A.A. The Effect of Ruthenium Promotion of the  $Co/\delta-Al_2O_3$  Catalyst on the Hydrogen Reduction Kinetics of Cobalt. *React. Kinet. Mech. Catal.* **2017**, *120*, 501–525. [[CrossRef](#)]
149. Phaahlamohlaka, T.N.; Dlamini, M.W.; Kumi, D.O.; Forbes, R.; Jewell, L.L.; Coville, N.J. Co inside Hollow Carbon Spheres as a Fischer–Tropsch Catalyst: Spillover Effects from Ru Placed inside and Outside the HCS. *Appl. Catal. Gen.* **2020**, *599*, 117617. [[CrossRef](#)]
150. Andreev, A.S.; Kazakova, M.A.; Ishchenko, A.V.; Selyutin, A.G.; Lapina, O.B.; Kuznetsov, V.L.; d’Espinose De La Cailleurie, J.-B. Magnetic and Dielectric Properties of Carbon Nanotubes with Embedded Cobalt Nanoparticles. *Carbon* **2017**, *114*, 39–49. [[CrossRef](#)]
151. Kazakova, M.A.; Andreev, A.S.; Selyutin, A.G.; Ishchenko, A.V.; Shubaev, A.V.; Kuznetsov, V.L.; Lapina, O.B.; d’Espinose De La Cailleurie, J.-B. Co Metal Nanoparticles Deposition inside or Outside Multi-Walled Carbon Nanotubes via Facile Support Pretreatment. *Appl. Surf. Sci.* **2018**, *456*, 657–665. [[CrossRef](#)]
152. Mohd Ridzuan, N.D.; Shaharun, M.S.; Anawar, M.A.; Ud-Din, I. Ni-Based Catalyst for Carbon Dioxide Methanation: A Review on Performance and Progress. *Catalysts* **2022**, *12*, 469. [[CrossRef](#)]
153. Strucks, P.; Failing, L.; Kaluza, S. A Short Review on Ni-Catalyzed Methanation of  $CO_2$ : Reaction Mechanism, Catalyst Deactivation, Dynamic Operation. *Chem. Ing. Tech.* **2021**, *93*, 1526–1536. [[CrossRef](#)]
154. Matsumura, Y.; Nakamori, T. Steam Reforming of Methane over Nickel Catalysts at Low Reaction Temperature. *Appl. Catal. Gen.* **2004**, *258*, 107–114. [[CrossRef](#)]
155. Vogt, C.; Kranenborg, J.; Monai, M.; Weckhuysen, B.M. Structure Sensitivity in Steam and Dry Methane Reforming over Nickel: Activity and Carbon Formation. *ACS Catal.* **2020**, *10*, 1428–1438. [[CrossRef](#)]
156. Hüfner, S. Electronic Structure of  $NiO$  and Related 3d-Transition-Metal Compounds. *Adv. Phys.* **1994**, *43*, 183–356. [[CrossRef](#)]
157. Noguera, C.; Mackrodt, W.C. Ab Initio Study of Ground and Excited States of  $NiO(100)$  Monolayer. *J. Phys. Condens. Matter* **2000**, *12*, 2163–2181. [[CrossRef](#)]
158. Rodriguez, J.A.; Hanson, J.C.; Frenkel, A.I.; Kim, J.Y.; Pérez, M. Experimental and Theoretical Studies on the Reaction of  $H_2$  with  $NiO$ : Role of O Vacancies and Mechanism for Oxide Reduction. *J. Am. Chem. Soc.* **2002**, *124*, 346–354. [[CrossRef](#)]
159. Borges, R.P.; Moura, L.G.; Kanitkar, S.; Spivey, J.J.; Noronha, F.B.; Hori, C.E. Hydrogen Production by Steam Reforming of Propane Using Supported Nickel over Ceria–Silica Catalysts. *Catal. Today* **2021**, *381*, 3–12. [[CrossRef](#)]
160. Shimoda, N.; Yoshimura, R.; Nukui, T.; Satokawa, S. Alloying Effect of Nickel–Cobalt Based Binary Metal Catalysts Supported on  $\alpha$ -Alumina for Ammonia Decomposition. *J. Chem. Eng. Jpn.* **2019**, *52*, 413–422. [[CrossRef](#)]
161. Theofanidis, S.-A.; Pieterse, J.A.Z.; Poelman, H.; Longo, A.; Sabbe, M.K.; Virginie, M.; Detavernier, C.; Marin, G.B.; Galvita, V.V. Effect of Rh in Ni-Based Catalysts on Sulfur Impurities during Methane Reforming. *Appl. Catal. B Environ.* **2020**, *267*, 118691. [[CrossRef](#)]
162. Fedorov, A.V.; Kukushkin, R.G.; Yeletsky, P.M.; Bulavchenko, O.A.; Chesalov, Y.A.; Yakovlev, V.A. Temperature-Programmed Reduction of Model  $CuO$ ,  $NiO$  and Mixed  $CuO$ – $NiO$  Catalysts with Hydrogen. *J. Alloys Compd.* **2020**, *844*, 156135. [[CrossRef](#)]
163. Bykova, M.V.; Ermakov, D.Y.; Kaichev, V.V.; Bulavchenko, O.A.; Saraev, A.A.; Lebedev, M.Y.; Yakovlev, V.A. Ni-Based Sol–Gel Catalysts as Promising Systems for Crude Bio-Oil Upgrading: Guaiacol Hydrodeoxygenation Study. *Appl. Catal. B Environ.* **2012**, *113–114*, 296–307. [[CrossRef](#)]
164. Kukushkin, R.G.; Bulavchenko, O.A.; Kaichev, V.V.; Yakovlev, V.A. Influence of Mo on Catalytic Activity of Ni-Based Catalysts in Hydrodeoxygenation of Esters. *Appl. Catal. B Environ.* **2015**, *163*, 531–538. [[CrossRef](#)]
165. Alekseeva, M.V.; Otyuskaya, D.S.; Rektina, M.A.; Bulavchenko, O.A.; Stonkus, O.A.; Kaichev, V.V.; Zavarukhin, S.G.; Thybaut, J.W.; Alexiadis, V.; Venderbosch, R.H.; et al. NiCuMo– $SiO_2$  Catalyst for Pyrolysis Oil Upgrading: Model Acidic Treatment Study. *Appl. Catal. Gen.* **2019**, *573*, 1–12. [[CrossRef](#)]
166. Alekseeva, M.V.; Gulyaeva, Y.K.; Bulavchenko, O.A.; Saraev, A.A.; Kremneva, A.M.; Stepanenko, S.A.; Koskin, A.P.; Kaichev, V.V.; Yakovlev, V.A. Promoting Effect of Zn in High-Loading Zn/Ni– $SiO_2$  Catalysts for Selective Hydrogen Evolution from Methylcyclohexane. *Dalton Trans.* **2022**, *51*, 6068–6085. [[CrossRef](#)]
167. Gulyaeva, Y.; Alekseeva, M.; Bulavchenko, O.; Kremneva, A.; Saraev, A.; Gerasimov, E.; Selishcheva, S.; Kaichev, V.; Yakovlev, V. Ni–Cu High-Loaded Sol–Gel Catalysts for Dehydrogenation of Liquid Organic Hydrides: Insights into Structural Features and Relationship with Catalytic Activity. *Nanomaterials* **2021**, *11*, 2017. [[CrossRef](#)]

168. Bulavchenko, O.A.; Smirnov, A.A.; Khromova, S.A.; Vinokurov, Z.S.; Ishchenko, A.V.; Yakovlev, V.A.; Tsybulya, S.V. In Situ Powder X-ray Diffraction Study of the Process of NiMoO<sub>4</sub>–SiO<sub>2</sub> Reduction with Hydrogen. *J. Struct. Chem.* **2016**, *57*, 955–961. [[CrossRef](#)]
169. Tichit, D.; Medina, F.; Coq, B.; Dutartre, R. Activation under Oxidizing and Reducing Atmospheres of Ni-Containing Layered Double Hydroxides. *Appl. Catal. Gen.* **1997**, *159*, 241–258. [[CrossRef](#)]
170. Ferreira, R.A.R.; Ávila-Neto, C.N.; Noronha, F.B.; Hori, C.E. Study of LPG Steam Reform Using Ni/Mg/Al Hydrotalcite-Type Precursors. *Int. J. Hydrogen Energy* **2019**, *44*, 24471–24484. [[CrossRef](#)]
171. Baraka, S.; Bouearan, K.; Caner, L.; Fontaine, C.; Epron, F.; Brahmi, R.; Bion, N. Catalytic Performances of Natural Ni-Bearing Clay Minerals for Production of Syngas from Dry Reforming of Methane. *J. CO<sub>2</sub> Util.* **2021**, *52*, 101696. [[CrossRef](#)]
172. Da Silva, B.C.; Bastos, P.H.C.; Junior, R.B.S.; Checca, N.R.; Costa, D.S.; Fréty, R.; Brandão, S.T. Oxy-CO<sub>2</sub> Reforming of CH<sub>4</sub> on Ni-Based Catalysts: Evaluation of Cerium and Aluminum Addition on the Structure and Properties of the Reduced Materials. *Catal. Today* **2021**, *381*, 50–64. [[CrossRef](#)]
173. Deka, D.J.; Kim, J.; Gunduz, S.; Aouine, M.; Millet, J.-M.M.; Co, A.C.; Ozkan, U.S. Investigation of Hetero-Phases Grown via in-Situ Exsolution on a Ni-Doped (La,Sr)FeO<sub>3</sub> Cathode and the Resultant Activity Enhancement in CO<sub>2</sub> Reduction. *Appl. Catal. B Environ.* **2021**, *286*, 119917. [[CrossRef](#)]
174. Marinho, A.L.A.; Rabelo-Neto, R.C.; Epron, F.; Bion, N.; Toniolo, F.S.; Noronha, F.B. Embedded Ni Nanoparticles in CeZrO<sub>2</sub> as Stable Catalyst for Dry Reforming of Methane. *Appl. Catal. B Environ.* **2020**, *268*, 118387. [[CrossRef](#)]
175. Zhang, F.; Liu, Z.; Chen, X.; Rui, N.; Betancourt, L.E.; Lin, L.; Xu, W.; Sun, C.; Abeykoon, A.M.M.; Rodriguez, J.A.; et al. Effects of Zr Doping into Ceria for the Dry Reforming of Methane over Ni/CeZrO<sub>2</sub> Catalysts: In Situ Studies with XRD, XAFS, and AP-XPS. *ACS Catal.* **2020**, *10*, 3274–3284. [[CrossRef](#)]
176. Rodriguez, J.A.; Hanson, J.C.; Stacchiola, D.; Senanayake, S.D. In Situ/Operando Studies for the Production of Hydrogen through the Water-Gas Shift on Metal Oxide Catalysts. *Phys. Chem. Chem. Phys.* **2013**, *15*, 12004. [[CrossRef](#)]
177. Zhu, M.; Rocha, T.C.R.; Lunkenbein, T.; Knop-Gericke, A.; Schlögl, R.; Wachs, I.E. Promotion Mechanisms of Iron Oxide-Based High Temperature Water-Gas Shift Catalysts by Chromium and Copper. *ACS Catal.* **2016**, *6*, 4455–4464. [[CrossRef](#)]
178. Li, S.; Krishnamoorthy, S.; Li, A.; Meitzner, G.D.; Iglesia, E. Promoted Iron-Based Catalysts for the Fischer-Tropsch Synthesis: Design, Synthesis, Site Densities, and Catalytic Properties. *J. Catal.* **2002**, *206*, 202–217. [[CrossRef](#)]
179. Schoch, R.; Huang, H.; Schünemann, V.; Bauer, M. A New Iron-Based Carbon Monoxide Oxidation Catalyst: Structure-Activity Correlation. *ChemPhysChem* **2014**, *15*, 3768–3775. [[CrossRef](#)] [[PubMed](#)]
180. Bukhtiyarova, G.A.; Bukhtiyarov, V.I.; Sakaeva, N.S.; Kaichev, V.V.; Zolotovskii, B.P. XPS Study of the Silica-Supported Fe-Containing Catalysts for Deep or Partial H<sub>2</sub>S Oxidation. *J. Mol. Catal. Chem.* **2000**, *158*, 251–255. [[CrossRef](#)]
181. Arabczyk, W.; Jasińska, I.; Lubkowski, K. The Surface Properties of Iron Catalyst for Ammonia Synthesis. *React. Kinet. Catal. Lett.* **2004**, *83*, 385–392. [[CrossRef](#)]
182. Jozwiak, W.K.; Kaczmarek, E.; Maniecki, T.P.; Ignaczak, W.; Manukiewicz, W. Reduction Behavior of Iron Oxides in Hydrogen and Carbon Monoxide Atmospheres. *Appl. Catal. Gen.* **2007**, *326*, 17–27. [[CrossRef](#)]
183. Nielsen, M.R.; Moss, A.B.; Bjørnlund, A.S.; Liu, X.; Knop-Gericke, A.; Klyushin, A.Y.; Grunwaldt, J.-D.; Sheppard, T.L.; Doronkin, D.E.; Zimina, A.; et al. Reduction and Carburization of Iron Oxides for Fischer-Tropsch Synthesis. *J. Energy Chem.* **2020**, *51*, 48–61. [[CrossRef](#)]
184. Zheng, Y.-F.; Liu, H.-Z.; Liu, Z.-J.; Li, X.-N. In Situ X-ray Diffraction Study of Reduction Processes of Fe<sub>3</sub>O<sub>4</sub>-and Fe<sub>1-x</sub>O-Based Ammonia-Synthesis Catalysts. *J. Solid State Chem.* **2009**, *182*, 2385–2391. [[CrossRef](#)]
185. Meshkani, F.; Rezaei, M. Preparation of Nanocrystalline Metal (Cr, Al, Mn, Ce, Ni, Co and Cu) Modified Ferrite Catalysts for the High Temperature Water Gas Shift Reaction. *Renew. Energy* **2015**, *74*, 588–598. [[CrossRef](#)]
186. Venugopal, A. Low Temperature Reductive Pretreatment of Au/Fe<sub>2</sub>O<sub>3</sub> Catalysts, TPR/TPO Studies and Behaviour in the Water-Gas Shift Reaction. *Appl. Catal. Gen.* **2004**, *258*, 241–249. [[CrossRef](#)]
187. Zhao, Z.; Tang, H.; Guo, Z. Effects of CaO on Precipitation Morphology of Metallic Iron in Reduction of Iron Oxides Under CO Atmosphere. *J. Iron Steel Res. Int.* **2013**, *20*, 16–24. [[CrossRef](#)]
188. Shi, B.; Zhang, Z.; Zha, B.; Liu, D. Structure Evolution of Spinel Fe-MII (M = Mn, Fe, Co, Ni) Ferrite in CO Hydrogenation. *Mol. Catal.* **2018**, *456*, 31–37. [[CrossRef](#)]
189. Niu, L.; Liu, X.; Wen, X.; Yang, Y.; Xu, J.; Li, Y. Effect of Potassium Promoter on Phase Transformation during H<sub>2</sub> Pretreatment of a Fe<sub>2</sub>O<sub>3</sub> Fischer Tropsch Synthesis Catalyst Precursor. *Catal. Today* **2020**, *343*, 101–111. [[CrossRef](#)]
190. Zhang, L.; Wang, H.; Yang, C.; Li, X.; Sun, J.; Wang, H.; Gao, P.; Sun, Y. The Rare Earth Elements Modified FeK/Al<sub>2</sub>O<sub>3</sub> Catalysts for Direct CO<sub>2</sub> Hydrogenation to Liquid Hydrocarbons. *Catal. Today* **2020**, *356*, 613–621. [[CrossRef](#)]
191. Yang, Z.; Luo, M.; Liu, Q.; Shi, B. In Situ XRD and Raman Investigation of the Activation Process over K–Cu–Fe/SiO<sub>2</sub> Catalyst for Fischer-Tropsch Synthesis Reaction. *Catal. Lett.* **2020**, *150*, 2437–2445. [[CrossRef](#)]
192. Bulavchenko, O.A.; Vinokurov, Z.S.; Saraev, A.A.; Tsapina, A.M.; Trigub, A.L.; Gerasimov, E.Y.; Gladky, A.Y.; Fedorov, A.V.; Yakovlev, V.A.; Kaichev, V.V. The Influence of Cu and Al Additives on Reduction of Iron(III) Oxide: In Situ XRD and XANES Study. *Inorg. Chem.* **2019**, *58*, 4842–4850. [[CrossRef](#)]
193. Saraev, A.A.; Tsapina, A.M.; Fedorov, A.V.; Trigub, A.L.; Bulavchenko, O.A.; Vinokurov, Z.S.; Zubavichus, Y.V.; Kaichev, V.V. CuFeAl-Composite Catalysts of Oxidation of Gasification Products of Solid Fuels: In Situ XAS and XRD Study. *Radiat. Phys. Chem.* **2020**, *175*, 108071. [[CrossRef](#)]

194. Grünbacher, M.; Schlicker, L.; Bekheet, M.F.; Gurlo, A.; Klötzer, B.; Penner, S. H<sub>2</sub> Reduction of Gd- and Sm-Doped Ceria Compared to Pure CeO<sub>2</sub> at High Temperatures: Effect on Structure, Oxygen Nonstoichiometry, Hydrogen Solubility and Hydroxyl Chemistry. *Phys. Chem. Chem. Phys.* **2018**, *20*, 22099–22113. [[CrossRef](#)]
195. Bekheet, M.F.; Grünbacher, M.; Schlicker, L.; Gili, A.; Doran, A.; Epping, J.D.; Gurlo, A.; Klötzer, B.; Penner, S. On the Structural Stability of Crystalline Ceria Phases in Undoped and Acceptor-Doped Ceria Materials under In Situ Reduction Conditions. *CrystEngComm* **2019**, *21*, 145–154. [[CrossRef](#)]
196. Ozawa, M.; Loong, C.-K. In Situ X-ray and Neutron Powder Diffraction Studies of Redox Behavior in CeO<sub>2</sub>-Containing Oxide Catalysts. *Catal. Today* **1999**, *50*, 329–342. [[CrossRef](#)]
197. Taira, K.; Murao, R. High Dispersion of CeO<sub>2</sub> on CeO<sub>2</sub>/MgO Prepared under Dry Conditions and Its Improved Redox Properties. *Energies* **2021**, *14*, 7922. [[CrossRef](#)]
198. Martínez-Munuera, J.C.; Giménez-Mañogil, J.; Castoldi, L.; Lietti, L.; García-García, A. Ceria-Based Catalysts for NO<sub>x</sub> Removal in NSR Processes: A Fundamental Study of the Catalyst Modifications Explored by In Situ Techniques. *Appl. Surf. Sci.* **2020**, *529*, 147019. [[CrossRef](#)]
199. Pakharukova, V.P.; Potemkin, D.I.; Stonkus, O.A.; Kharchenko, N.A.; Saraev, A.A.; Gorlova, A.M. Investigation of the Structure and Interface Features of Ni/Ce<sub>1-x</sub>Zr<sub>x</sub>O<sub>2</sub> Catalysts for CO and CO<sub>2</sub> Methanation. *J. Phys. Chem. C* **2021**, *125*, 20538–20550. [[CrossRef](#)]
200. Zhang, F.; Yao, S.; Liu, Z.; Gutiérrez, R.A.; Vovchok, D.; Cen, J.; Xu, W.; Ramírez, P.J.; Kim, T.; Senanayake, S.D.; et al. Reaction of Methane with MO<sub>x</sub>/CeO<sub>2</sub> (M = Fe, Ni, and Cu) Catalysts: In Situ Studies with Time-Resolved X-ray Diffraction. *J. Phys. Chem. C* **2018**, *122*, 28739–28747. [[CrossRef](#)]
201. Wang, X.; Rodriguez, J.A.; Hanson, J.C.; Gamarra, D.; Martínez-Arias, A.; Fernández-García, M. In Situ Studies of the Active Sites for the Water Gas Shift Reaction over Cu–CeO<sub>2</sub> Catalysts: Complex Interaction between Metallic Copper and Oxygen Vacancies of Ceria. *J. Phys. Chem. B* **2006**, *110*, 428–434. [[CrossRef](#)] [[PubMed](#)]
202. Bulavchenko, O.A.; Afonasenko, T.N.; Osipov, A.R.; Pochtar, A.A.; Saraev, A.A.; Gerasimov, E.Y. The Formation of Mn-Ce Oxide Catalysts for CO Oxidation by Oxalate Route: The Role of Annealing Conditions. *Catal. Lett.* **2021**, *151*, 2906–2918. [[CrossRef](#)]
203. Rodriguez, J.A.; Rui, N.; Zhang, F.; Senanayake, S.D. In Situ Studies of Methane Activation Using Synchrotron-Based Techniques: Guiding the Conversion of C–H Bonds. *ACS Catal.* **2022**, *12*, 5470–5488. [[CrossRef](#)]
204. Zhang, F.; Liu, Z.; Zhang, S.; Akter, N.; Palomino, R.M.; Vovchok, D.; Orozco, I.; Salazar, D.; Rodriguez, J.A.; Llorca, J.; et al. In Situ Elucidation of the Active State of Co–CeO<sub>x</sub> Catalysts in the Dry Reforming of Methane: The Important Role of the Reducible Oxide Support and Interactions with Cobalt. *ACS Catal.* **2018**, *8*, 3550–3560. [[CrossRef](#)]
205. Wang, H.; Srinath, N.V.; Poelman, H.; Detavernier, C.; Li, P.; Marin, G.B.; Galvita, V.V. Hierarchical Fe-Modified MgAl<sub>2</sub>O<sub>4</sub> as a Ni-Catalyst Support for Methane Dry Reforming. *Catal. Sci. Technol.* **2020**, *10*, 6987–7001. [[CrossRef](#)]
206. Marin, C.M.; Popczun, E.J.; Nguyen-Phan, T.-D.; Tafen, D.N.; Alfonso, D.; Waluyo, I.; Hunt, A.; Kauffman, D.R. Designing Perovskite Catalysts for Controlled Active-Site Exsolution in the Microwave Dry Reforming of Methane. *Appl. Catal. B Environ.* **2021**, *284*, 119711. [[CrossRef](#)]
207. Liu, Z.; Zhang, F.; Rui, N.; Li, X.; Lin, L.; Betancourt, L.E.; Su, D.; Xu, W.; Cen, J.; Attenkofer, K.; et al. Highly Active Ceria-Supported Ru Catalyst for the Dry Reforming of Methane: In Situ Identification of Ru<sup>δ+</sup>–Ce<sup>3+</sup> Interactions for Enhanced Conversion. *ACS Catal.* **2019**, *9*, 3349–3359. [[CrossRef](#)]
208. Bekheet, M.F.; Delir Kheyrollahi Nezhad, P.; Bonmassar, N.; Schlicker, L.; Gili, A.; Praetz, S.; Gurlo, A.; Doran, A.; Gao, Y.; Heggen, M.; et al. Steering the Methane Dry Reforming Reactivity of Ni/La<sub>2</sub>O<sub>3</sub> Catalysts by Controlled In Situ Decomposition of Doped La<sub>2</sub>NiO<sub>4</sub> Precursor Structures. *ACS Catal.* **2021**, *11*, 43–59. [[CrossRef](#)]
209. Liu, Z.; Yao, S.; Johnston-Peck, A.; Xu, W.; Rodriguez, J.A.; Senanayake, S.D. Methanol Steam Reforming over Ni-CeO<sub>2</sub> Model and Powder Catalysts: Pathways to High Stability and Selectivity for H<sub>2</sub>/CO<sub>2</sub> Production. *Catal. Today* **2018**, *311*, 74–80. [[CrossRef](#)]
210. Zhou, G.; Barrio, L.; Agnoli, S.; Senanayake, S.D.; Evans, J.; Kubacka, A.; Estrella, M.; Hanson, J.C.; Martínez-Arias, A.; Fernández-García, M.; et al. High Activity of Ce<sub>1-x</sub>Ni<sub>x</sub>O<sub>2-y</sub> for H<sub>2</sub> Production through Ethanol Steam Reforming: Tuning Catalytic Performance through Metal-Oxide Interactions. *Angew. Chem. Int. Ed.* **2010**, *49*, 9680–9684. [[CrossRef](#)] [[PubMed](#)]
211. Clausen, B. In Situ Cell for Combined XRD and On-Line Catalysis Tests: Studies of Cu-Based Water Gas Shift and Methanol Catalysts. *J. Catal.* **1991**, *132*, 524–535. [[CrossRef](#)]
212. Si, R.; Tao, J.; Evans, J.; Park, J.B.; Barrio, L.; Hanson, J.C.; Zhu, Y.; Hrbek, J.; Rodriguez, J.A. Effect of Ceria on Gold–Titania Catalysts for the Water–Gas Shift Reaction: Fundamental Studies for Au/CeO<sub>x</sub>/TiO<sub>2</sub> (110) and Au/CeO<sub>x</sub>/TiO<sub>2</sub> Powders. *J. Phys. Chem. C* **2012**, *116*, 23547–23555. [[CrossRef](#)]
213. Patlolla, A.; Carino, E.V.; Ehrlich, S.N.; Stavitski, E.; Frenkel, A.I. Application of Operando XAS, XRD, and Raman Spectroscopy for Phase Speciation in Water Gas Shift Reaction Catalysts. *ACS Catal.* **2012**, *2*, 2216–2223. [[CrossRef](#)]
214. Vovchok, D.; Guild, C.J.; Dissanayake, S.; Llorca, J.; Stavitski, E.; Liu, Z.; Palomino, R.M.; Waluyo, I.; Li, Y.; Frenkel, A.I.; et al. In Situ Characterization of Mesoporous Co/CeO<sub>2</sub> Catalysts for the High-Temperature Water-Gas Shift. *J. Phys. Chem. C* **2018**, *122*, 8998–9008. [[CrossRef](#)]
215. López Cámará, A.; Cortés Corberán, V.; Martínez-Arias, A.; Barrio, L.; Si, R.; Hanson, J.C.; Rodriguez, J.A. Novel Manganese-Promoted Inverse CeO<sub>2</sub>/CuO Catalyst: In Situ Characterization and Activity for the Water-Gas Shift Reaction. *Catal. Today* **2020**, *339*, 24–31. [[CrossRef](#)]

216. Barrio, L.; Kubacka, A.; Zhou, G.; Estrella, M.; Martínez-Arias, A.; Hanson, J.C.; Fernández-García, M.; Rodriguez, J.A. Unusual Physical and Chemical Properties of Ni in  $\text{Ce}_{1-x}\text{Ni}_x\text{O}_{2-y}$  Oxides: Structural Characterization and Catalytic Activity for the Water Gas Shift Reaction. *J. Phys. Chem. C* **2010**, *114*, 12689–12697. [[CrossRef](#)]
217. Zhu, M.; Chen, J.; Shen, L.; Ford, M.E.; Gao, J.; Xu, J.; Wachs, I.E.; Han, Y.-F. Probing the Surface of Promoted  $\text{CuO-Cr}_2\text{O}_3-\text{Fe}_2\text{O}_3$  Catalysts during  $\text{CO}_2$  Activation. *Appl. Catal. B Environ.* **2020**, *271*, 118943. [[CrossRef](#)]
218. Wang, J.; Liu, C.-Y.; Senftle, T.P.; Zhu, J.; Zhang, G.; Guo, X.; Song, C. Variation in the  $\text{In}_2\text{O}_3$  Crystal Phase Alters Catalytic Performance toward the Reverse Water Gas Shift Reaction. *ACS Catal.* **2020**, *10*, 3264–3273. [[CrossRef](#)]
219. Lin, L.; Yao, S.; Rui, N.; Han, L.; Zhang, F.; Gerlak, C.A.; Liu, Z.; Cen, J.; Song, L.; Senanayake, S.D.; et al. Conversion of  $\text{CO}_2$  on a Highly Active and Stable  $\text{Cu}/\text{FeO}_x/\text{CeO}_2$  Catalyst: Tuning Catalytic Performance by Oxide-Oxide Interactions. *Catal. Sci. Technol.* **2019**, *9*, 3735–3742. [[CrossRef](#)]
220. Muhler, M. The Nature of the Iron Oxide-Based Catalyst for Dehydrogenation of Ethylbenzene to Styrene I. Solid-State Chemistry and Bulk Characterization. *J. Catal.* **1990**, *126*, 339–360. [[CrossRef](#)]
221. Gao, Y.; Wang, X.; Liu, J.; Huang, C.; Zhao, K.; Zhao, Z.; Wang, X.; Li, F. A Molten Carbonate Shell Modified Perovskite Redox Catalyst for Anaerobic Oxidative Dehydrogenation of Ethane. *Sci. Adv.* **2020**, *6*, eaaz9339. [[CrossRef](#)] [[PubMed](#)]
222. Zhu, X.; Gao, Y.; Wang, X.; Haribal, V.; Liu, J.; Neal, L.M.; Bao, Z.; Wu, Z.; Wang, H.; Li, F. A Tailored Multi-Functional Catalyst for Ultra-Efficient Styrene Production under a Cyclic Redox Scheme. *Nat. Commun.* **2021**, *12*, 1329. [[CrossRef](#)]
223. Wei, Z.; Shao, F.; Wang, J. Recent Advances in Heterogeneous Catalytic Hydrogenation and Dehydrogenation of N-Heterocycles. *Chin. J. Catal.* **2019**, *40*, 980–1002. [[CrossRef](#)]
224. Li, Y.; Wu, Z. A Review of In Situ/Operando Studies of Heterogeneous Catalytic Hydrogenation of  $\text{CO}_2$  to Methanol. *Catal. Today* **2023**, *420*, 114029. [[CrossRef](#)]
225. Mishchenko, D.D.; Vinokurov, Z.S.; Afonasenko, T.N.; Saraev, A.A.; Simonov, M.N.; Gerasimov, E.Y.; Bulavchenko, O.A. Insights into the Contribution of Oxidation-Reduction Pretreatment for  $\text{Mn}_{0.2}\text{Zr}_{0.8}\text{O}_{2-\delta}$  Catalyst of CO Oxidation Reaction. *Materials* **2023**, *16*, 3508. [[CrossRef](#)]
226. Bulavchenko, O.A.; Vinokurov, Z.S.; Afonasenko, T.N.; Gerasimov, E.Y.; Konovalova, V.P. The Activation of  $\text{MnO}_x\text{-ZrO}_2$  Catalyst in CO Oxidation: Operando XRD Study. *Mater. Lett.* **2022**, *315*, 131961. [[CrossRef](#)]
227. Bulavchenko, O.A.; Vinokurov, Z.S.; Konovalova, V.P.; Afonasenko, T.N. OPERANDO X-RAY DIFFRACTION ANALYSIS OF THE  $\text{MnO}_x\text{-ZrO}_2$  CATALYST DURING OXIDATION OF PROPANE. *J. Struct. Chem.* **2022**, *63*, 885–894. [[CrossRef](#)]
228. Lashina, E.A.; Vinokurov, Z.S.; Saraev, A.A.; Kaichev, V.V. Self-Sustained Oscillations in Oxidation of Methane over Palladium: Experimental Study and Mathematical Modeling. *J. Chem. Phys.* **2022**, *157*, 044703. [[CrossRef](#)]
229. Kaichev, V.V.; Vinokurov, Z.S.; Saraev, A.A. Self-Sustained Oscillations in Oxidation of Methane over Palladium: The Nature of “Low-Active” and “Highly Active” States. *Catal. Sci. Technol.* **2021**, *11*, 4392–4397. [[CrossRef](#)]
230. Strong, P.J.; Xie, S.; Clarke, W.P. Methane as a Resource: Can the Methanotrophs Add Value? *Environ. Sci. Technol.* **2015**, *49*, 4001–4018. [[CrossRef](#)] [[PubMed](#)]
231. Schwach, P.; Pan, X.; Bao, X. Direct Conversion of Methane to Value-Added Chemicals over Heterogeneous Catalysts: Challenges and Prospects. *Chem. Rev.* **2017**, *117*, 8497–8520. [[CrossRef](#)] [[PubMed](#)]
232. Lavoie, J.-M. Review on Dry Reforming of Methane, a Potentially More Environmentally-Friendly Approach to the Increasing Natural Gas Exploitation. *Front. Chem.* **2014**, *2*, 81. [[CrossRef](#)] [[PubMed](#)]
233. Mondal, K.; Sasimal, S.; Badgandi, S.; Chowdhury, D.R.; Nair, V. Dry Reforming of Methane to Syngas: A Potential Alternative Process for Value Added Chemicals—A Techno-Economic Perspective. *Environ. Sci. Pollut. Res.* **2016**, *23*, 22267–22273. [[CrossRef](#)]
234. Gili, A.; Schlicker, L.; Bekheet, M.F.; Görke, O.; Penner, S.; Grünbacher, M.; Götsch, T.; Littlewood, P.; Marks, T.J.; Stair, P.C.; et al. Surface Carbon as a Reactive Intermediate in Dry Reforming of Methane to Syngas on a 5% Ni/MnO Catalyst. *ACS Catal.* **2018**, *8*, 8739–8750. [[CrossRef](#)]
235. Bartholomew, C.H. Mechanisms of Catalyst Deactivation. *Appl. Catal. Gen.* **2001**, *212*, 17–60. [[CrossRef](#)]
236. Argyle, M.; Bartholomew, C. Heterogeneous Catalyst Deactivation and Regeneration: A Review. *Catalysts* **2015**, *5*, 145–269. [[CrossRef](#)]
237. Svintsitskiy, D.A.; Kardash, T.Y.; Lazareva, E.V.; Saraev, A.A.; Derevyannikova, E.A.; Vorokhta, M.; Šmíd, B.; Bondareva, V.M. NAP-XPS and In Situ XRD Study of the Stability of Bi-Modified  $\text{MoVNbTeO}$  Catalysts for Oxidative Dehydrogenation of Ethane. *Appl. Catal. Gen.* **2019**, *579*, 141–150. [[CrossRef](#)]
238. Muhler, M. The Nature of the Iron Oxide-Based Catalyst for Dehydrogenation of Ethylbenzene to Styrene 2. Surface Chemistry of the Active Phase. *J. Catal.* **1992**, *138*, 413–444. [[CrossRef](#)]
239. Muhler, M.; Schlögl, R.; Reller, A.; Ertl, G. The Nature of the Active Phase of the Fe/K-Catalyst for Dehydrogenation of Ethylbenzene. *Catal. Lett.* **1989**, *2*, 201–210. [[CrossRef](#)]
240. Guan, C.; Liu, Z.; Wang, D.; Zhou, X.; Pang, Y.; Yu, N.; Van Bavel, A.P.; Vovk, E.; Yang, Y. Exploring the Formation of Carbonates on  $\text{La}_2\text{O}_3$  Catalysts with OCM Activity. *Catal. Sci. Technol.* **2021**, *11*, 6516–6528. [[CrossRef](#)]
241. Moura, L.G.; Borges, R.P.; Noronha, F.B.; Hori, C.E. Steam Reforming of Liquefied Petroleum Gas Using Catalysts Supported on Ceria-Silica. *Int. J. Hydrogen Energy* **2021**, *46*, 1801–1814. [[CrossRef](#)]
242. Vamvakeros, A.; Matras, D.; Jacques, S.D.M.; Di Michiel, M.; Middelkoop, V.; Cong, P.; Price, S.W.T.; Bull, C.L.; Senecal, P.; Beale, A.M. Real-Time Tomographic Diffraction Imaging of Catalytic Membrane Reactors for the Oxidative Coupling of Methane. *Catal. Today* **2021**, *364*, 242–255. [[CrossRef](#)]

243. Kim, I.S.; Li, Z.; Zheng, J.; Platero-Prats, A.E.; Mavrandonakis, A.; Pellizzeri, S.; Ferrandon, M.; Vjunov, A.; Gallington, L.C.; Webber, T.E.; et al. Sinter-Resistant Platinum Catalyst Supported by Metal–Organic Framework. *Angew. Chem. Int. Ed.* **2018**, *57*, 909–913. [[CrossRef](#)] [[PubMed](#)]
244. Fichtl, M.B.; Schlereth, D.; Jacobsen, N.; Kasatkin, I.; Schumann, J.; Behrens, M.; Schlögl, R.; Hinrichsen, O. Kinetics of Deactivation on Cu/ZnO/Al<sub>2</sub>O<sub>3</sub> Methanol Synthesis Catalysts. *Appl. Catal. Gen.* **2015**, *502*, 262–270. [[CrossRef](#)]
245. Sadeghi, S.; Vafajoo, L.; Kazemeini, M.; Fattahi, M. Modeling of the Methanol Synthesis Catalyst Deactivation in a Spherical Bed Reactor: An Environmental Challenge. *APCBEE Procedia* **2014**, *10*, 84–90. [[CrossRef](#)]
246. Zhang, F.; Xu, X.; Qiu, Z.; Feng, B.; Liu, Y.; Xing, A.; Fan, M. Improved Methanol Synthesis Performance of Cu/ZnO/Al<sub>2</sub>O<sub>3</sub> Catalyst by Controlling Its Precursor Structure. *Green Energy Environ.* **2022**, *7*, 772–781. [[CrossRef](#)]
247. Zarabi Golkhatmi, S.; Asghar, M.I.; Lund, P.D. A Review on Solid Oxide Fuel Cell Durability: Latest Progress, Mechanisms, and Study Tools. *Renew. Sustain. Energy Rev.* **2022**, *161*, 112339. [[CrossRef](#)]
248. Mishchenko, D.D.; Arapova, M.V.; Bespalko, Y.N.; Vinokurov, Z.S.; Shmakov, A.N. In Situ XRD and TGA/DTA Study of Multiphase La- and Nd-Substituted Pr<sub>2</sub>NiO<sub>4</sub> under IT-SOFC Cathode Operating Conditions. *J. Alloys Compd.* **2023**, *967*, 171693. [[CrossRef](#)]
249. Popov, M.P.; Bychkov, S.F.; Bulina, N.V.; Nemudry, A.P. In Situ High-Temperature X-ray Diffraction of Hollow Fiber Membranes under Operating Conditions. *J. Eur. Ceram. Soc.* **2019**, *39*, 1717–1720. [[CrossRef](#)]
250. Liu, Y.; Zhu, X.; Yang, W. Degradation Mechanism Analysis of Ba<sub>0.5</sub>Sr<sub>0.5</sub>Co<sub>0.8</sub>Fe<sub>0.2</sub>O<sub>3-δ</sub> Membranes at Intermediate-Low Temperatures. *AIChE J.* **2015**, *61*, 3879–3888. [[CrossRef](#)]
251. Nikolaeva, O.; Kapišnikov, A.; Gerasimov, E. Structural Insight into La<sub>0.5</sub>Ca<sub>0.5</sub>Mn<sub>0.5</sub>Co<sub>0.5</sub>O<sub>3</sub> Decomposition in the Methane Combustion Process. *Nanomaterials* **2021**, *11*, 2283. [[CrossRef](#)] [[PubMed](#)]
252. Heenan, T.M.M.; Robinson, J.B.; Lu, X.; Tjaden, B.; Cervellino, A.; Bailey, J.J.; Brett, D.J.L.; Shearing, P.R. Understanding the Thermo-Mechanical Behaviour of Solid Oxide Fuel Cell Anodes Using Synchrotron X-ray Diffraction. *Solid State Ion.* **2018**, *314*, 156–164. [[CrossRef](#)]
253. Li, T.; Heenan, T.M.M.; Rabuni, M.F.; Wang, B.; Farandos, N.M.; Kelsall, G.H.; Matras, D.; Tan, C.; Lu, X.; Jacques, S.D.M.; et al. Design of Next-Generation Ceramic Fuel Cells and Real-Time Characterization with Synchrotron X-ray Diffraction Computed Tomography. *Nat. Commun.* **2019**, *10*, 1497. [[CrossRef](#)]

**Disclaimer/Publisher’s Note:** The statements, opinions and data contained in all publications are solely those of the individual author(s) and contributor(s) and not of MDPI and/or the editor(s). MDPI and/or the editor(s) disclaim responsibility for any injury to people or property resulting from any ideas, methods, instructions or products referred to in the content.